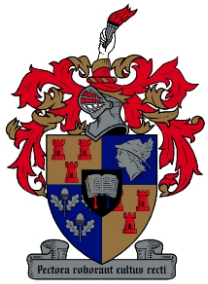

UNIVERSITEIT • STELLENBOSCH • UNIVERSITY

On the hydrodynamic permeability of foamlike media

by

Josefine Wilms

Thesis presented at the University of Stellenbosch in partial fulfilment of the requirements for the degree of

Master of Engineering Science

Department of Applied Mathematics
University of Stellenbosch
Private Bag X1, 7602 Matieland, South Africa

Study leader: Prof J.P. Du Plessis

April 2006

Declaration

I, the undersigned, hereby declare that the work contained in this thesis is my own original work and that I have not previously in its entirety or in part submitted it at any university for a degree.

Signature: .....
J.M. Wilms

Date: .....

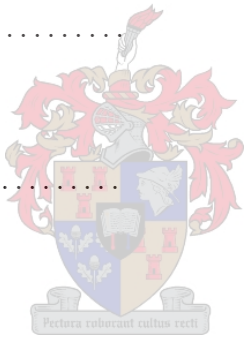

Abstract

This work entails the improvement of an existing three dimensional pore-scale model. Stagnant zones are included, the closure of the volume averaged pressure gradient is improved and an improved calculation of pore-scale averages, using the RUC, is done for the model to be a more realistic representative of the REV and thus of the foamlike material. Both the Darcy and the Forchheimer regimes are modelled and a general momentum transport equation is derived by means of an asymptotic matching technique. The RUC model is also extended to cover non-Newtonian flow. Since metallic foams are generally of porosities greater than 90%, emphasis is put on the accurate prediction of permeability for these porosities. In order to improve permeability predictions for these high porosity cases an adaptation to the RUC model was considered, whereby rectangular prisms were replaced by cylinders. Although this adaptation appears to give more accurate permeabilities at very high porosities, its implementation in a generalised model seems impractical. The prediction of the characteristic RUC side length is discussed and results of both the cylindrical strand model and the square strand model are compared to experimental work.

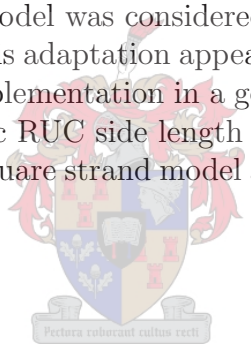

Opsomming

Hierdie werk behels die verbetering van 'n bestaande drie dimensionele VES (verteenwoordigende eenheidssel) model. Voorsiening is gemaak vir stagnante sones, die berekening van die volume-gemiddelde drukgradiënt is verbeter asook 'n verskuiwing van die VES tydens berekeninge is gedoen ten einde die model meer verteenwoordigend van die VEV (Verteenwoordigende eenheidsvolume) en gevolglik die sponsagtige materiaal te maak. Die Darcy en die Forchheimer vloeiverskynsels word gemodelleer en 'n algemene momentum transport vergelyking daargestel deur van 'n asimptotiese passingstegniek gebruik te maak. Die model is uitgebrei vir nie-Newton vloei. Klem word gelê op akkurate permeabiliteitsvoorspelling vir porositeite groter as 90%, siende dat die porositeit van metaal sponse gewoonlik hierdie gebied beslaan. 'n Nuwe model is ontwikkel om beter voorspellings vir hoë porositeite te bewerkstellig. Die reghoekige prismas van die VES word vervang deur silinders en 'n model word ontwikkel om die permeabiliteit te voorspel. Vir baie hoë porositeite gee hierdie model verbeterde voorspellings van permeabiliteit. Die implementering daarvan in 'n veralgemeende model skyn egter onprakties te wees. Die vasstelling van die karakteristieke VES-sylengte word bespreek en resultate van beide die silindriese model, en die VES model word met eksperimentele data vergelyk.

Acknowledgements

I would like to thank the following:

- Professor du Plessis for his support and constant motivation. He is an exceptional teacher.
- My parents for always having confidence in me.
- Gerhard Venter for helping me with LaTeX.

Contents

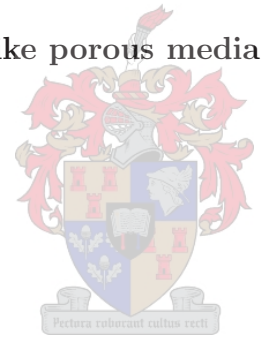

Nomenclature

Standard characters

a	$[m]$	Diagonal cell size
C	$[Pa]$	Absolute viscosity for power-law fluid
d	$[m]$	Linear RRUC dimension
d_c	$[m]$	Linear CRUC dimension
d_f	$[m]$	RRUC pore width
dm	$[\mu m]$	arithmetic mean of strand diameter
f_b	$[m.s^{-2}]$	Gravitational acceleration
F_C	$[m^{-2}]$	Friction factor for cylinder model
F_R	$[m^{-2}]$	Friction factor for RUC model
k	$[m^2]$	Hydrodynamic permeability
K	[ ]	Dimensionless hydrodynamic permeability
k_{oz}	[ ]	Kozeny constant
L	$[m]$	Predefined straight line length
L_e	$[m]$	Length of tortuous flow path for displacement L
m	$[m]$	Hydraulic radius
n	[ ]	Power-law constant
$\underline{\widehat{n}}$	[]	Unit vector in streamwise direction
p	$[Pa]$	Pressure
p_f	$[Pa]$	$\langle p \rangle_f$ = Intrinsic average fluid pressure
$\underline{q}$	$[m/s]$	Darcy velocity, Streamwise superficial velocity
Q	$[m^3/s]$	Flow rate
S	$[m^2]$	Surface
S_{ff}	$[m^2]$	Fluid-fluid Interface

S_{fs}	$[m^2]$	Fluid-solid Interface
S_g	$[m^2]$	S_{fs} of U_g
$S_{\|\|}$	$[m^2]$	S_{fs} of $U_{\|\|}$
$S_\perp$	$[m^2]$	S_{fs} of $U_\perp$
$\underline{u}$	$[m/s]$	Drift velocity
U_f	$[m^3]$	RRUC fluid volume
$\mathcal{U}_f$	$[m^3]$	REV fluid volume
U_g	$[m^3]$	RRUC stagnant volume
U_o	$[m^3]$	RRUC volume
$\mathcal{U}_o$	$[m^3]$	REV volume
U_s	$[m^3]$	RRUC solid volume
$\mathcal{U}_s$	$[m^3]$	REV solid volume
U_t	$[m^3]$	RRUC transfer volume
$U_\perp$	$[m^3]$	RRUC perpendicular volume
$U_{\|\|}$	$[m^3]$	RRUC streamwise volume
$\underline{v}$	$[m/s]$	Actual velocity field
$\underline{w}$	$[m/s]$	Streamwise channel velocity

Greek symbols

β	[ ]	Velocity ratio
δ	$[m]$	RRUC_g solid width
ϵ	[ ]	Porosity, $\frac{\mathcal{U}_f}{\mathcal{U}_o}$
η	$[m]$	Passability
μ	$[N \cdot s/m^2]$	Fluid dynamic viscosity
ρ	$[kg/m^3]$	Fluid density
τ	$[N/m^2]$	Local shear stress
χ	[ ]	Tortuosity
ψ	[ ]	Intrinsic streamwise volume fraction

Miscellaneous

$\langle\ \rangle$	Phase average operator
$\langle\ \rangle_f$	Intrinsic phase average operator
^{o}	Deviation operator
∇	Del operator

Acronyms

CRUC	Cylindrical representative unit cell
REV	Representative elementary volume
RRUC	Rectangular representative unit cell

Subscripts

$\|\|$	Parallel to streamwise direction
$\perp$	Perpendicular to streamwise direction
f	Fluid matter
ff	Fluid-fluid interface
fs	Fluid-solid interface
g	Stagnant
o	Total solid and fluid volume
s	Solid matter
t	Transfer
g	Granular

Chapter 1

Introduction

Cellular metallic foams have become increasingly popular for flow control and heat transfer enhancement due to their intricate interfacial geometry and particularly high surface area per unit volume. Such foams have recently become commercially available and their use in industrial engineering processes is rapidly increasing.

Since these processes have to be optimised for maximal gain, the proper understanding of, and knowledge about the underlying physical phenomena of fluid and gas transport in such foams are of paramount importance. Mathematical models are thus needed to predict and analyse such phenomena.

Du Plessis & Masliyah (1988) introduced a geometrical model characterising the microstructure of foam by the rectangular distribution of solid material in a representative unit cell or RUC shown in Figure 1.1. This model was then improved on by Du Plessis et al. (1994) and applied to predict the pressure drop through high porosity metallic foams for the flow of water and glycerol with considerable success. The characteristic length, d, of the RUC however still had to be determined experimentally.

Fourie & Du Plessis (2001) enhanced the modelling procedure of Du Plessis et al. (1994) by developing an analytical expression for the characteristic dimension, d, of the RUC as a function of two measurable geometrical parameters, namely cell size and porosity. A tetrakaidecahedronal shape was introduced to approximate the geometry of a single cell. The resulting analytical expression for the RUC-width, was

$$d \approx 0.57a \tag{1.1}$$

where a is the cell size. The 1994 model, however, provided a similar result by simply using the cell size, a, of the RUC model shown in Figure 1.1. The relation between the RUC side length, d, and the diagonal cell size, a, is

$$d = \frac{a}{\sqrt{3}} \approx 0.58a. \tag{1.2}$$

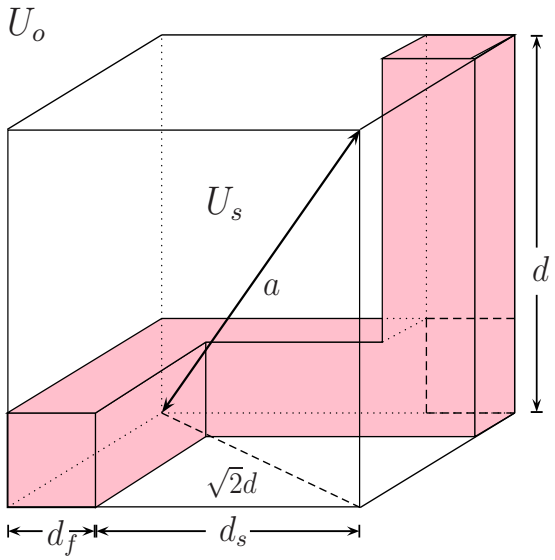

Figure 1.1: RUC cell size, a.

The introduction of the tetradekaihedronal shape therefore appears redundant in this respect since the relation between the characteristic side length, d, and cell size, a, could have been determined without it. Also, the particular tetragon shape can only be used with considerable difficulty in further generalisation of the model.

The model to be developed in this work is an extension of research done by Du Plessis et al. (1994). This work, however, differs from the former in two ways. Firstly, following a method applied by Lloyd et al. (2004) for two dimensions, modelling is done over all possible RRUC's in order to be a better representative of an REV and therefore the foamlike material. Secondly, the RUC is modified to include stagnant regions.

The model developed in this work was already used extensively in the work to be reported by Crosnier et al. (2006). In the present work analytical expressions for the characteristic RUC side length, d, and the drag coefficient, c_d, are developed. The present modelling of the inertial term differs slightly from that done by Crosnier et al. (2006) and these differences are discussed. Close correlation is achieved between the present theoretical model and experimental data for pressure drop in high porosity aluminium (ERG) foams.

The present model is also extended for the prediction of the permeability for the discharge of a particular non-Newtonian flow in metallic foams, (Smit et al. (2005)), (Appendix E).

In Chapter 4 an adaptation to the RUC model is considered, namely replacing the rectangular prisms by cylinders, to determine the accuracy of this work in case of high porosities.

Chapter 2

Volume averaging theory

Integral calculus of continuum fields is normally used to mathematically analyse fluid motion of a single phase fluid. In case of single phase flow phenomena in porous media an adaptation of calculus to include two phases is necessary since the differential volume element, dU, is required to contain both phases and cannot be assumed to shrink to zero in the limit, as is implied in ordinary differential calculus.

During the past 30 years a general theory of volume averaging has been developed (for more detail see e.g. Bear & Bachmat (1991), Whitaker (1996)). The main aspects of the development needed for this study are outlined in this chapter.

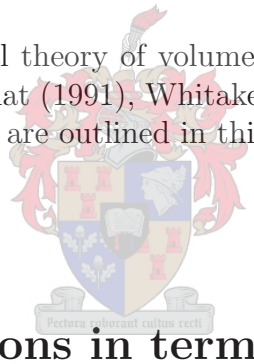

2.1 General definitions in terms of an REV

At each point, $\underline{r}_o$, in the porous domain, the continuum volumetric differential element is replaced by a representative elementary volume (REV) of finite extent and with centroid at the particular point. It must be large enough to contain sufficient solid and fluid parts to be statistically representative of the average geometric properties of the porous domain. The REV must, however, also be small enough, relative to the large scale boundaries of the porous medium, to function implicitly as a differential element.

Figure 2.1 is a schematic of an REV of volume, $\mathcal{U}_o$. The solid and fluid volumes within $\mathcal{U}_o$ are respectively denoted by $\mathcal{U}_s$ and $\mathcal{U}_f$, with $\mathcal{S}_{fs}$ denoting the fluid-solid surface interface between them. That part of the boundary of $\mathcal{U}_f$ which is in contact with fluid particles outside the REV is denoted by $\mathcal{S}_{ff}$.

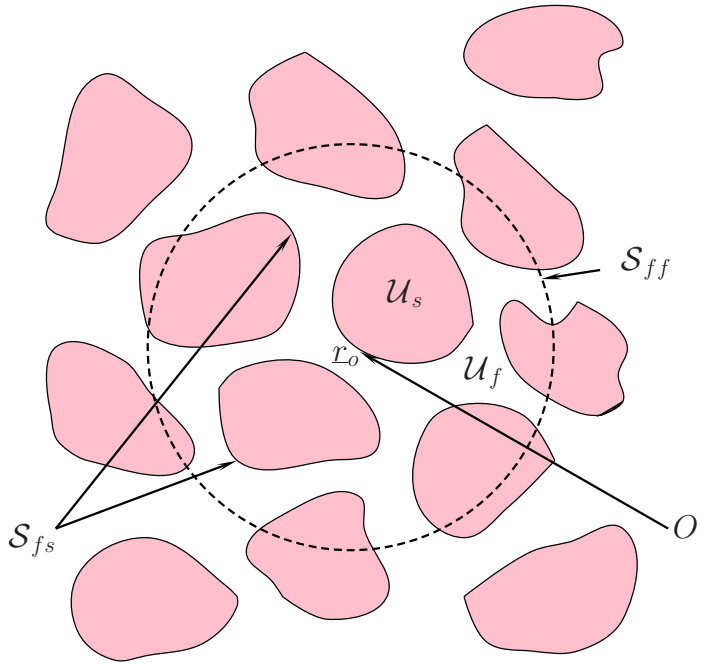

Figure 2.1: Representative Elementary Volume relative to a fixed origin O.

The volume $\mathcal{U}_o$ of the REV may thus be written as:

$$\mathcal{U}_o \;=\; \mathcal{U}_s \;+\; \mathcal{U}_f. \tag{2.1}$$

The fluid phase average of any quantity ψ is defined by

$$\langle\psi\rangle \;\equiv\; \frac{1}{\mathcal{U}_o} \iiint\limits_{\mathcal{U}_f} \psi \, d\mathcal{U} \tag{2.2}$$

and the intrinsic fluid phase average of ψ by

$$\langle\psi\rangle_f \;\equiv\; \frac{1}{\mathcal{U}_f} \iiint\limits_{\mathcal{U}_f} \psi \, d\mathcal{U}. \tag{2.3}$$

The deviation, $\{\psi\}$, of a parameter, ψ, at any point, is defined as

$$\{\psi\} \;\equiv \psi - \langle\psi\rangle_f \,. \tag{2.4}$$

The porosity (void fraction), ϵ, of any foam is defined as the phase average of unity, namely

$$\epsilon \equiv \langle 1 \rangle = \frac{\mathcal{U}_f}{\mathcal{U}_o}. \tag{2.5}$$

The porosity is an important parameter in the mathematical description of flow in porous media.

2.2 Velocity definitions

The actual velocity field, $\underline{v}$, of the fluid within $\mathcal{U}_f$ is denoted by

$$\underline{v} = v\, \underline{\widetilde{n}}, \tag{2.6}$$

where $\underline{\widetilde{n}}$ is a dimensionless unit vector field that is parallel to the actual velocity vector at each point in $\mathcal{U}_f$. The phase average of the actual velocity gives the superficial or Darcy velocity and is defined as

$$\underline{q} \equiv \langle \underline{v} \rangle = \frac{1}{\mathcal{U}_o} \iiint_{\mathcal{U}_f} \underline{v}\, d\mathcal{U}. \tag{2.7}$$

The direction of $\underline{q}$ is called the *streamwise direction* and is denoted by the vector field $\underline{\widehat{n}}$, so that

$$\underline{q} = q\, \underline{\widehat{n}}. \tag{2.8}$$

The intrinsic phase average of the actual velocity gives the *drift velocity* and is defined as

$$\underline{u} \equiv \langle \underline{v} \rangle_f = \frac{1}{\mathcal{U}_f} \iiint_{\mathcal{U}_f} \underline{v}\, d\mathcal{U} = \underline{q}/\epsilon. \tag{2.9}$$

This relationship was introduced by Dupuit-Forchheimer, (e.g. Carman (1937)). The *streamwise channel velocity*, $\underline{w}$, was introduced by Diedericks & Du Plessis (1995) and is defined as

$$\underline{w} \equiv \frac{1}{\mathcal{U}_{\mathcal{L}}} \iiint_{\mathcal{U}_f} \underline{v}\, d\mathcal{U}, \tag{2.10}$$

where the streamwise volume, $\mathcal{U}_{\mathcal{L}}$, is the volume available for streamwise displacement of the fluid and is defined by

$$\mathcal{U}_{\mathcal{L}} \equiv \iiint_{\mathcal{U}_f} \underline{\tilde{n}} \cdot \underline{\hat{n}} \, d\mathcal{U}. \tag{2.11}$$

2.3 Volume averaged transport equations

For the present work the interstitial fluid is assumed to be stationary incompressible and Newtonian. The flow is thus governed by the continuity equation,

$$\nabla \cdot \underline{v} = 0 \tag{2.12}$$

and the Navier-Stokes equation,

$$\rho \nabla \cdot \underline{v}\,\underline{v} = \rho \underline{f}_b - \nabla p + \mu \nabla^2 \underline{v}. \tag{2.13}$$

Volume averaging of equations (2.12) and (2.13) leads to the following averaged continuity equation:

$$\nabla \cdot \underline{q} = 0 \tag{2.14}$$

and the averaged Navier-Stokes equation:

$$\begin{aligned} \rho \nabla \cdot (\underline{q}\,\underline{q}/\epsilon) + \nabla \cdot \left(\epsilon \left\langle \mathring{\underline{v}}\,\mathring{\underline{v}} \right\rangle_f \right) = \epsilon \rho \underline{f}_b - \epsilon \nabla p_f + \mu \nabla^2 \underline{q} \\ - \frac{1}{\mathcal{U}_o} \iint_{\mathcal{S}_{fs}} \underline{n} \, \mathring{p} \, d\mathcal{S} + \frac{1}{\mathcal{U}_o} \iint_{\mathcal{S}_{fs}} \underline{n} \cdot \underline{\underline{\tau}} \, d\mathcal{S}. \end{aligned} \tag{2.15}$$

If the averaged flow field, $\underline{q}$, is assumed to be uniform and the porosity constant, equation (2.15) reduces to

$$-\epsilon \nabla \langle p \rangle_f = \frac{1}{\mathcal{U}_o} \iint_{\mathcal{S}_{fs}} \underline{n} p \, d\mathcal{S} - \frac{1}{\mathcal{U}_o} \iint_{\mathcal{S}_{fs}} \mu \underline{n} \cdot \nabla \underline{v} \, d\mathcal{S}. \tag{2.16}$$

Equation (2.16) is still open in the sense that it contains the pore-scale parameters p and $\nabla \underline{v}$ which must be resolved at each point on S_{fs}. Closure modelling for particular porous structures to transform equation (2.16) into an equation with only macroscopic (average) parameters, is discussed in the next section.

2.4 Existing model

An overview of the method followed to close equation (2.16) up until 2004 is given in the following section. Equation (2.16) can be written in terms of the viscous stress dyad:

$$-\epsilon\nabla\langle p\rangle_f = \frac{1}{\mathcal{U}_o}\iint_{\mathcal{S}_{fs}} \underline{n}p\,d\mathcal{S} - \frac{1}{\mathcal{U}_o}\iint_{\mathcal{S}_{fs}} \underline{n}\cdot\underline{\underline{\tau}}\,d\mathcal{S}. \tag{2.17}$$

A dimensionless criterion which determines the relative importance of inertial and viscous effects is the Reynolds number:

$$Re = \frac{\text{Inertia forces}}{\text{Viscous forces}}. \tag{2.18}$$

Situations in which the Reynolds number is small are called slow viscous flows. Viscous forces arising from shearing motions of the fluid predominate over inertial forces associated with acceleration or deceleration of fluid particles. As the Reynolds number increases the inertial forces become more important relative to the viscous forces until the Forchheimer regime is reached when the inertial forces predominate. At very high Reynolds numbers the flow becomes turbulent, i.e., time dependent fluctuations occur. For the present, only viscous flow will be taken into consideration and "high Reynolds numbers" will refer to the upper limit of Reynolds numbers for where the flow is still purely laminar. Typically this limit will be in the 100-500 range, depending on the definition of Re.

2.4.1 Viscous flow

The fluid-solid interface in equation (2.17) is partitioned into parallel and transverse regions:

$$\begin{aligned}-\epsilon\nabla\langle p\rangle_f = {} & \frac{1}{\mathcal{U}_o}\iint_{\mathcal{S}_{||}} \underline{n}\,p\,d\mathcal{S} + \frac{1}{\mathcal{U}_o}\iint_{\mathcal{S}_{\perp}} \underline{n}\,p\,d\mathcal{S} \\ & -\frac{1}{\mathcal{U}_o}\iint_{\mathcal{S}_{||}} \underline{n}\cdot\underline{\underline{\tau}}\,d\mathcal{S} - \underline{\frac{1}{\mathcal{U}_o}\iint_{\mathcal{S}_{\perp}} \underline{n}\cdot\underline{\underline{\tau}}\,d\mathcal{S}}.\end{aligned} \tag{2.19}$$

The streamwise portion of the pressure integral is zero due to symmetry cancellations. The underlined section has no streamwise component and disappears seeing that the left side of our equation is in the streamwise direction. For very small Reynolds numbers the pressure difference between the transverse faces are very small. This term therefore is

dropped and the lost information incorporated by integrating the wall shear stress over the total solid-fluid interface. This is achieved by numerically forcing the contribution of the transverse part into the streamwise direction, namely

$$-\epsilon\nabla\left\langle p\right\rangle_f \;=\; -\frac{1}{\mathcal{U}_o}\iint\limits_{\mathcal{S}_{||}} \underline{n}\cdot\underline{\tau}\,d\mathcal{S} - \widehat{\underline{n}}\frac{1}{\mathcal{U}_o}\iint\limits_{\mathcal{S}_{\perp}} \underline{n}\cdot\underline{\tau}\cdot\widetilde{\underline{n}}\,d\mathcal{S}. \tag{2.20}$$

The wall shear stress, τ_w, is now assumed uniform and constant over the whole of S_{fs},

$$-\epsilon\nabla\left\langle p\right\rangle_f \;=\; \widehat{\underline{n}}\frac{1}{\mathcal{U}_o}\iint\limits_{\mathcal{S}_{fs}} \tau_w\,d\mathcal{S}. \tag{2.21}$$

Plane Poiseuille flow is assumed for a pore width, d_p, and an average interstitial velocity, v_p. In so doing equation (2.21) renders

$$-\epsilon\nabla\left\langle p\right\rangle_f \;=\; \left(\frac{S_{||}+S_{\perp}}{U_o}\right)\left(\frac{6\mu v_p}{d_p}\right)\widehat{\underline{n}} \;=\; \frac{S_{||}+S_{\perp}}{U_o}\frac{6}{d_p}\left(\frac{\chi}{\epsilon}\right)\mu\,\underline{q}. \tag{2.22}$$

The definition of hydrodynamic permeability is given in one dimensional form by,

$$k \;\equiv\; \frac{\mu\,\underline{q}}{-\frac{d\left\langle p\right\rangle_f}{dx}}. \tag{2.23}$$

Since the pressure differences only occur in the streamwise direction,

$$-\nabla\left\langle p\right\rangle_f \equiv \frac{d\left\langle p\right\rangle_f}{dx}. \tag{2.24}$$

Since we have established in equation (2.22) that

$$-\frac{d\left\langle p\right\rangle_f}{dx} \;=\; \frac{1}{\epsilon}\frac{S_{||}+S_{\perp}}{U_o}\frac{6}{d_p}\left(\frac{\chi}{\epsilon}\right)\mu\,\underline{q}, \tag{2.25}$$

the permeability can now be written in the following closed form:

$$k \;=\; \frac{U_o d_p \epsilon^2}{6\chi\left(S_{||}+S_{\perp}\right)}. \tag{2.26}$$

This expression for the permeability is general and can be applied to all porous media. Its particular application to foamlike media is described in the following sections.

2.5 Improved model

2.5.1 Closure modelling with an RRUC

A closure modelling procedure, that aims to approximate the porous material by imbedding the average geometric characteristics of the material as found in an REV within the smallest possible hypothetical *rectangular representative unit cell* (RRUC), was proposed by Du Plessis & Masliyah (1988). The RRUC provides a facility to consider flow conditions within a most elementary control volume, U_o, model of the particular porous medium. This representation should be interpreted as a certain arrangement of solid material to fulfil the basic requirements of the average geometry of the actual porous structure it resembles. The RRUC is restricted to rectangular geometry and it thus generally takes on the shape of a rectangular block. The restriction to rectangular RRUC's is only for geometrical simplicity and may be relaxed, although with substantial increase in algebraic complexity. The porosity of the RRUC must be the same as that of the REV it represents, so that, analogous to equation (2.5):

$$\epsilon = \frac{U_f}{U_o}. \tag{2.27}$$

In Figure 2.2 the geometry of an RRUC for a foamlike material introduced by Du Plessis & Masliyah (1988) is shown. The shaded volume represents the void part contained within a cube of side length, d.

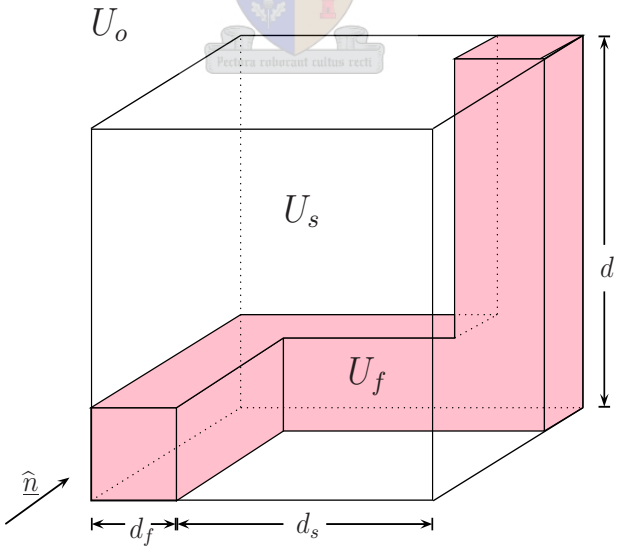

Figure 2.2: Geometry of RRUC model for an isotropic metallic foam ($\epsilon \approx 0.2$).

The configuration in Figure 2.2 is drawn for a porosity of about 0.2. From equation (2.27) the porosity of the model in Figure 2.2 can be expressed in terms of the RRUC parameters as

$$\epsilon \;=\; \frac{3d_f^2 d - 2d_f^3}{d^3} \;=\; \left(\frac{d_f}{d}\right)^2 \left(3 - 2\frac{d_f}{d}\right). \tag{2.28}$$

Here d_f represents the normal distance between any two facing solid surfaces in a channel.

The fundamental approach for the analytical modelling is the assumption of a rectangular morphology for the interstitial solid distribution and interstitially fully developed viscous flow between each and every pair of "parallel plates" within the RRUC. Time-independent, piece-wise plane Poiseuille flow is thus assumed as interstitial flow condition. If w is the average velocity in the channel between the plates, the pressure gradient is given by

$$-\nabla p \;=\; \frac{12\mu w}{(d_f)^2}. \tag{2.29}$$

2.5.2 Volume partitioning within an RRUC

At any point within the foam the RRUC is set up with one channel parallel to the streamwise direction, $\underline{\widehat{n}}$, for the REV at that particular point as is shown in Figure 2.3. Since the flow in this streamwise directed channel is in the direction of $\underline{q}$ the streamwise volume is given by

$$U_{||} \;\equiv\; d_f^2(d - d_f). \tag{2.30}$$

The transit volume, needed to carry the fluid, in the streamwise direction, through to the opposite side of the RRUC, is given by

$$U_t \;\equiv\; d_f^3. \tag{2.31}$$

Fluid in other channels of the RRUC may either be stagnant or it flows *transverse*, that is to say, perpendicular to the streamwise direction. If we denote by $U_\perp$ the total volume where transverse motion takes place and by U_g the volume of stagnant regions within the RRUC,

$$U_\perp \;+\; U_g \;=\; 2U_{||} \tag{2.32}$$

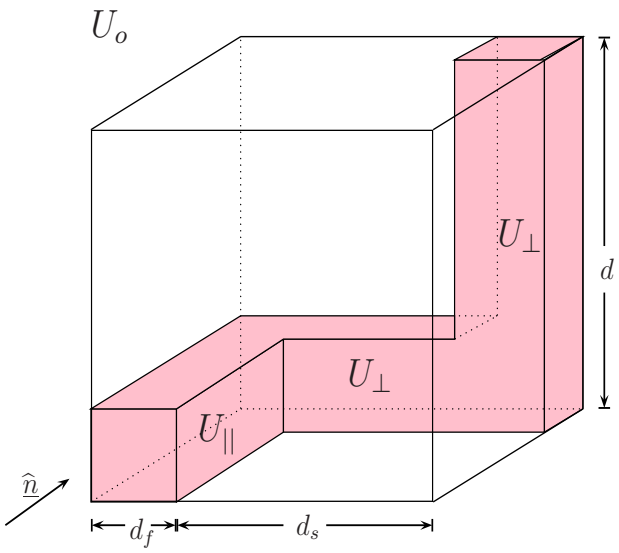

Figure 2.3: Geometry of RRUC model for an isotropic metallic foam ($\epsilon \approx 0.2$).

in magnitude and it follows that

$$U_f \;=\; U_{||} + U_t + U_\perp + U_g \;=\; 3U_{||} + U_t. \tag{2.33}$$

From equation (2.27) the porosity can be expressed in terms of these volumes as

$$\epsilon \;=\; \frac{U_{||} + U_t + U_\perp + U_g}{U_{||} + U_t + U_\perp + U_g + U_s} \;=\; \frac{3U_{||} + U_t}{3U_{||} + U_t + U_s}. \tag{2.34}$$

A geometrical factor, the *intrinsic streamwise volume fraction* , ψ, which is the fraction of the void volume that is available for streamwise transport of fluid, is defined by:

$$\psi \;\equiv\; \frac{U_f}{U_{||} + U_t} \;=\; \frac{U_{||} + U_t + U_\perp + U_g}{U_{||} + U_t}. \tag{2.35}$$

Since in all cases $U_{||} + U_t + U_g \;=\; 3U_{||}$, the factor ψ may be now be evaluated as follows:

$$\psi = \;\frac{3U_{||} + U_t}{U_{||} + U_t} = \frac{3d_f^2(d - d_f) + d_f^3}{d_f^2(d - d_f) + d_f^3} \;=\; 3 - 2\frac{d_f}{d}. \tag{2.36}$$

It thus follows that

$$\frac{d_f}{d} \;=\; \frac{3 - \psi}{2} \tag{2.37}$$

and

$$\frac{d_s}{d} \;=\; \frac{\psi - 1}{2}. \tag{2.38}$$

If the result of equation (2.38) is substituted in equation (A.6) it follows that,

$$\psi^3 - 6\psi^2 + 9\psi - 4\epsilon \;=\; 0 \tag{2.39}$$

subject to the constraint that

$$\psi \;=\; 1 \;\text{ if }\; \epsilon \;=\; 1. \tag{2.40}$$

The solution to equation (2.39) and condition (2.40) is

$$\psi \;=\; 2 + 2\cos\left[\frac{4\pi + \cos^{-1}(2\epsilon - 1)}{3}\right] \tag{2.41}$$

and this expression is presented graphically in Figure 2.4.

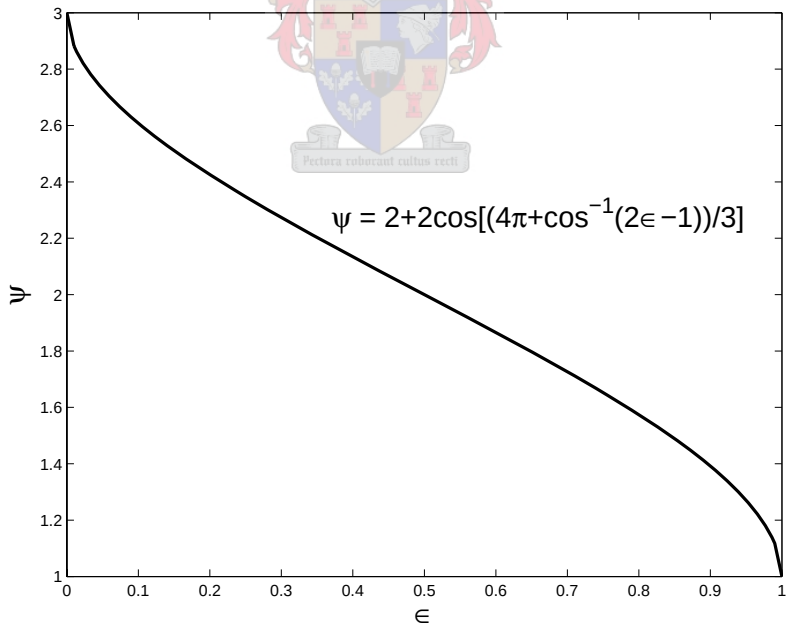

Figure 2.4: The intrinsic streamwise volume fraction, ψ, as a function of porosity (equation (2.41)).

2.5.3 Surfaces of the RRUC

The fluid-solid surfaces can be written as follows in terms of the edge lengths of the RRUC,

$$S_{fs} = 12d_f(d - d_f). \tag{2.42}$$

In substituting equations (2.37) and (2.38) into equation (2.42), it follows that,

$$S_{fs} = 3d^2(\psi - 1)(3 - \psi). \tag{2.43}$$

The surfaces of the streamwise volume can be expressed in terms of edge lengths as,

$$S_{||} = 4d_f(d - d_f). \tag{2.44}$$

Substituting equations (2.37) and (2.38) into equation (2.44) gives,

$$S_{||} = d^2(\psi - 1)(3 - \psi). \tag{2.45}$$

In the absence of stagnant regions, $S_\perp$, is written in terms of RRUC edges as,

$$S_\perp = 8d_f(d - d_f). \tag{2.46}$$

Again applying equations (2.37) and (2.38) to the above, results in the following:

$$S_\perp = 2d^2(\psi - 1)(3 - \psi) \tag{2.47}$$

In the absence of stagnant volumes,

$$S_g = 0. \tag{2.48}$$

2.5.4 Velocity relationships

Global preservation of streamwise mass flow implies that flow through the d_f^2 plane at velocity, $\underline{w}$, equals flow through the d^2 plane at the Darcy velocity, $\underline{q}$. This implies that,

$$\underline{w}d_f^2 = \underline{q}d^2. \tag{2.49}$$

Rewriting equation (2.49) and using equation (A.6) it follows that,

$$\underline{w} \;=\; \underline{q}\frac{d^2}{d_f^2} \;=\; \frac{\underline{q}}{\epsilon}\left(3 - 2\frac{d_f}{d}\right). \tag{2.50}$$

Following equations (2.36) and (2.35) the streamwise channel velocity can thus be expressed as,

$$\underline{w} \;=\; \frac{\underline{q}\psi}{\epsilon} \;=\; \frac{\underline{q}}{\epsilon}\frac{U_f}{U_{||} + U_t}. \tag{2.51}$$

It thus appears that the geometrical factor, ψ, plays a fundamental role in the prediction of permeability. Equation (2.51) holds even if there are stagnant regions in the flow domain.

2.5.5 Volume averaging of the pressure gradient

In this section an approach similar to that of Lloyd et al. (2004) for 2D structures will be followed to obtain closure for the pressure gradient for a three-dimensional foamlike structure. As such it forms an elaboration of a presentation at an international conference, Wilms et al. (2005), attached as Appendix E.

If the volume averaging is performed over an RRUC and a uniform average flow field is assumed, the flow through a foam is governed by the continuity equation (2.12):

$$\nabla\cdot\,\underline{q} \;=\; 0 \tag{2.52}$$

and the following form of the averaged Navier-Stokes equation (2.16):

$$-\,\nabla\langle p\rangle \;=\; \frac{1}{U_o}\iint\limits_{S_{fs}} \underline{n}\,p\,dS \;-\; \frac{1}{U_o}\iint\limits_{S_{fs}} \underline{n}\cdot\underline{\tau}\,dS. \tag{2.53}$$

These two equations may now be 'closed' for a particular foam by the introduction of a particular RRUC, resembling the average properties of the foam geometry, and within which the surface integrals are to be evaluated.

Following Lloyd et al. (2004), the two integrals in equation (2.53) are split into streamwise and transverse integrals, yielding

$$
\begin{aligned}
-\nabla\langle p\rangle = \; & \underline{\frac{1}{U_o}\iint\limits_{S_{||}} \underline{n}\, p\, dS} + \frac{1}{U_o}\iint\limits_{S_\perp} \underline{n}\, p\, dS \\
& - \frac{1}{U_o}\iint\limits_{S_{||}} \underline{n}\cdot\underline{\underline{\tau}}\, dS - \underline{\frac{1}{U_o}\iint\limits_{S_\perp} \underline{n}\cdot\underline{\underline{\tau}}\, dS}
\end{aligned}
\tag{2.54}
$$

of which the underlined integrals are zero. In the remaining pressure integral, for each transverse channel section, the pressure is split into a channel wall average pressure, $\overline{p_w}$, and a wall pressure deviation, $\widetilde{p_w}$, yielding,

$$
-\nabla\langle p\rangle = \frac{1}{U_o}\iint\limits_{S_\perp} \underline{n}\,\overline{p_w}\, dS + \frac{1}{U_o}\iint\limits_{S_\perp} \underline{n}\,\widetilde{p_w}\, dS - \frac{1}{U_o}\iint\limits_{S_{||}} \underline{n}\cdot\underline{\underline{\tau}}\, dS. \tag{2.55}
$$

In evaluating the perpendicular surface integrals, the integral over all possible RRUC's must be taken to comply with the notion that an RRUC is a proper substitute for an REV. In other words, the integral should be done over an REV, i.e. over a number of RUC's randomly cut by the outer boundary of the REV. Since the pressure equation at hand is streamwise, this will only effect integration over $S_\perp$ planes.

In Figure 2.5 the notation followed here is shown schematically. Let the integrals over S_{AA} and S_{BB} respectively denote a surface integral over a cell of which the walls cut through solid parts as shown by the dashed lines A, and a second integral where the cell walls do not cut though any solid as shown by the dashed lines B. The average wall pressure integrals need to be weighed according to their relative frequency of occurrence. This need not be done with the parallel surfaces or pressure deviation on perpendicular surfaces, since a shift in the streamwise direction does not result in any loss of friction. It follows that,

$$
\begin{aligned}
-\nabla\langle p\rangle = \; & \underline{\frac{d_s}{d}\cdot\frac{1}{U_o}\iint\limits_{S_{AA}} \underline{n}\,\overline{p_w}\, dS} + \frac{d-d_s}{d}\cdot\frac{1}{U_o}\iint\limits_{S_{BB}} \underline{n}\,\overline{p_w}\, dS \\
& + \frac{1}{U_o}\iint\limits_{S_\perp} \underline{n}\,\widetilde{p_w}\, dS - \frac{1}{U_o}\iint\limits_{S_{||}} \underline{n}\cdot\underline{\underline{\tau}}\, dS.
\end{aligned}
\tag{2.56}
$$

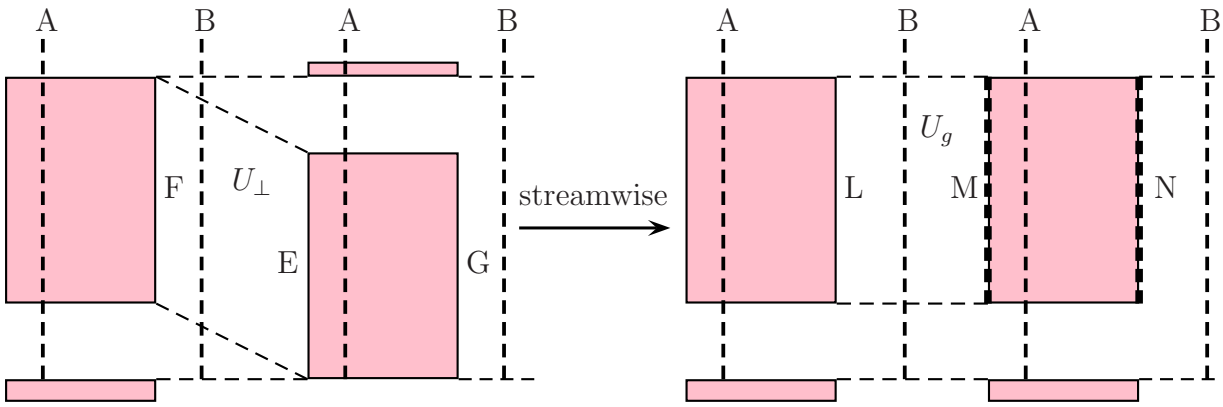

(a) Overstaggered array (b) Regular array

Figure 2.5: Schematic for the evaluation of surface integrals.

The underlined integral is zero since $\overline{p_w}$ is from definition equal for walls E and F and for walls L and M. The pressure deviations are caused by shear stress at the transverse surfaces and the pressure deviation integral thus provides the streamwise effect of the transverse integral omitted from equation (2.54). Together the last two integrals thus equal the total pressure drop caused by all shear stresses. This allows us to write

$$-\nabla\langle p\rangle = \frac{d_f}{d}\cdot\frac{1}{U_o}\iint\limits_{S_{BB}} \underline{n\,\overline{p_w}}\,dS + \frac{\tau_{||}S_{||}+\tau_\perp S_\perp}{U_o}\,\widehat{\underline{n}}, \tag{2.57}$$

where $\tau_{||}$ and $\tau_\perp$ is the wall shear stress respectively in the streamwise and transverse channels. It should be noted here that for each RRUC in the BB-range of the foam structure there are two transverse channels. Referring to Figure 2.6, $\nabla\langle p\rangle$ can be written as follows,

$$\nabla\langle p\rangle = \frac{\langle p\rangle_A - \langle p\rangle_B}{\delta_{AB}}. \tag{2.58}$$

Here $\langle p\rangle_A$ and $\langle p\rangle_B$ are the average pressures in the A and B RUC's respectively and δ_{AB} the distance between the centers of these RUC's. Letting δp be the loss in pressure as a result of friction on the parallel edges and applying averaging, the above can be written as follows in terms of RUC subvolumes:

$$\begin{aligned}\nabla\langle p\rangle = {} & \frac{\overline{p_w}(U_g+U_t)+(\overline{p_w}-\frac{1}{2}\delta\overline{p_w})U_{||}}{U_o d} \\ & -\frac{\left[(\overline{p_w}+\delta\overline{p_w})(U_g+U_t)+(\overline{p_w}+\frac{1}{2}\delta\overline{p_w})U_{||}\right]}{U_o d}.\end{aligned} \tag{2.59}$$

Simplifying and taking into account the definition of porosity, the following relationship can be derived between $\nabla \langle p \rangle$ and $\delta\overline{p_w}$:

$$\nabla \langle p \rangle = -\epsilon \frac{\delta \overline{p_w}}{d}. \tag{2.60}$$

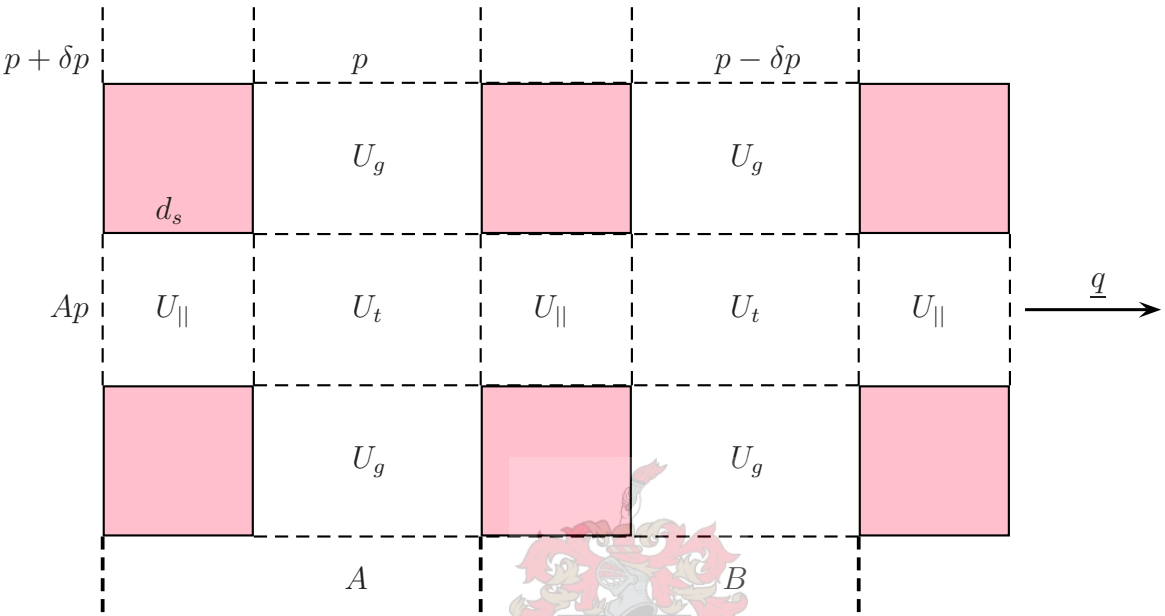

Figure 2.6: Evaluation of average pressure gradients.

This relationship enables the remaining surface integral in equation(2.57) to be written as follows in terms of RUC volumes:

$$\frac{d_f}{d}\frac{1}{U_o} \iint\limits_{S_{BB}} \underline{n}\overline{p_w} dS = \frac{d_f}{d}\frac{1}{U_o}\left[\iint\limits_{S_{BB}\ EG} \underline{n}\overline{p_w}\, dS + \iint\limits_{S_{BB}\ MN} \underline{n}\overline{p_w}\, dS \right] \tag{2.61}$$

$$= \frac{d_f}{d}\frac{1}{U_o}\left[\widehat{\underline{n}}\delta_{EG}\overline{p_w} + \widehat{\underline{n}}\delta_{MN}\overline{p_w}\right] \tag{2.62}$$

$$= \frac{d_f}{d}\frac{1}{U_o}\delta\overline{p_w}(d_\perp + d_g)d \tag{2.63}$$

$$= -\frac{d_f d(d_\perp + d_g)}{U_o}\nabla \langle p \rangle_f \tag{2.64}$$

$$= -\frac{U_\perp + U_g}{U_f}\nabla \langle p\rangle \tag{2.65}$$

$$= -\frac{U_f - (U_{||} + U_t)}{U_f}\nabla \langle p\rangle \tag{2.66}$$

$$= \left[\frac{U_{||} + U_t}{U_f} - 1\right]\nabla \langle p\rangle . \tag{2.67}$$

Equation (2.57) can therefore be expressed as follows:

$$-\nabla\langle p\rangle = \frac{\tau_{||}S_{||} + \tau_\perp S_\perp}{U_o}\,\underline{\widehat{n}} + \left(\frac{U_{||} + U_t}{U_f} - 1\right)\nabla \langle p\rangle . \tag{2.68}$$

Combining the gradient of pressure terms yields

$$-\frac{U_{||} + U_t}{U_f}\,\nabla\langle p\rangle = \frac{\tau_{||}S_{||} + \tau_\perp S_\perp}{U_o}\,\underline{\widehat{n}}, \tag{2.69}$$

that is to say

$$-\nabla\langle p\rangle = \frac{U_f}{U_{||} + U_t}\cdot\frac{\tau_{||}S_{||} + \tau_\perp S_\perp}{U_o}\,\underline{\widehat{n}}. \tag{2.70}$$

If $w_{||}$ and $w_\perp$ are the channel average velocities in $U_{||}$ and $U_\perp$ respectively, the interstitial channel average velocity ratio, β, may be defined as

$$\beta \equiv \frac{w_\perp}{w_{||}}. \tag{2.71}$$

The following is then obtained

$$-\nabla\langle p\rangle = \frac{S_{||} + \beta S_\perp}{U_o}\cdot\left(\frac{U_f}{U_{||} + U_t}\right)^2\cdot\frac{6\mu\,\underline{q}}{\epsilon d_f} \tag{2.72}$$

and this leads to the gradient of the intrinsic phase average for the pressure of

$$-\nabla\langle p\rangle_f = \frac{S_{||} + \beta S_\perp}{U_o}\cdot\left(\frac{U_f}{U_{||} + U_t}\right)^2\cdot\frac{6\mu\,\underline{q}}{\epsilon^2 d_f}. \tag{2.73}$$

The hydrodynamic permeability for any of the structures considered is thus given by

$$k \equiv \frac{\mu\,\underline{q}}{|\nabla\langle p\rangle_f|} = \frac{U_o}{S_{||} + \beta S_\perp}\cdot\left(\frac{U_{||} + U_t}{U_f}\right)^2\cdot\frac{\epsilon^2 d_f}{6} \tag{2.74}$$

and the dimensionless hydrodynamic permeability by:

$$K \equiv \frac{k}{d^2} = \frac{\epsilon^2 d^2}{6(S_{||} + \beta S_{\perp})} \cdot \left(\frac{U_{||} + U_t}{U_f} \right)^2 \cdot \frac{d_f}{d}. \tag{2.75}$$

The permeability is thus expressed entirely in terms of the geometric features of the porous domain.

2.5.6 RRUC models allowing stagnant regions

Presented in Figures 2.7, 2.8 and 2.9 are representations of three RRUC models, respectively for over-staggered, fully staggered and non-staggered configurations. The hydrodynamic permeability, k, is to be determined for each of these as a single-valued function of porosity only.

Over-staggered model

In case of the over-staggered model the fluid is assumed to traverse all three void channels as is shown in Figure 2.7, without any stagnant regions.

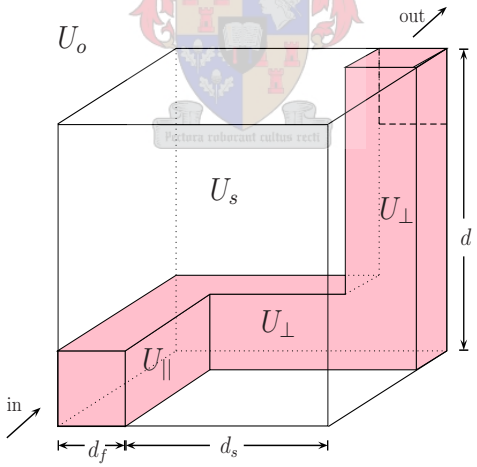

Figure 2.7: RRUC for the over-staggered foam model.

The hydrodynamic permeability and dimensionless hydrodynamic permeability for the over-staggered case can thus be written as a function of ϵ and ψ as follows,

$$k = \frac{\epsilon^2 d^2}{36\psi^2(\psi - 1)} \tag{2.76}$$

and

$$K = \frac{\epsilon^2}{36\psi^2(\psi - 1)}. \tag{2.77}$$

Equation (2.77) is graphically represented in Figure 2.10, to follow.

Fully staggered model

In case of the fully staggered model, one of the three void arms of the RUC contains stagnant fluid and is thus a dead zone as is shown in Figure 2.8.

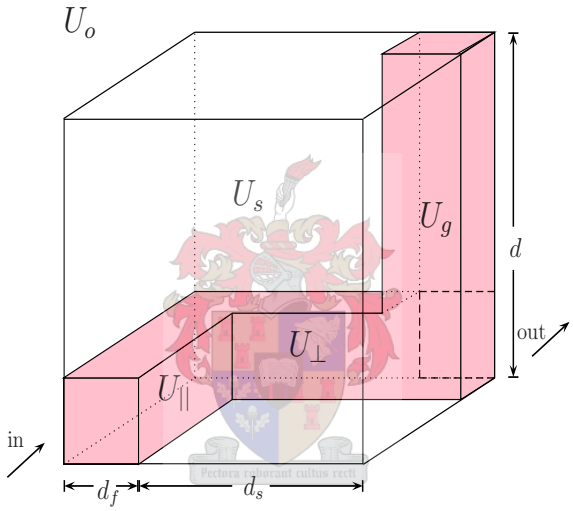

Figure 2.8: RRUC for the fully staggered foam model.

By applying equations (2.74) and (2.75) the hydrodynamic permeability and dimensionless hydrodynamic permeability for the fully staggered case can be written as a function of ϵ and ψ as follows,

$$k = \frac{\epsilon^2 d^2}{24\psi^2(\psi - 1)} \tag{2.78}$$

and

$$K = \frac{\epsilon^2}{24\psi^2(\psi - 1)}. \tag{2.79}$$

Equation (2.79) is graphically represented in Figure 2.10, to follow.

Non-staggered model

In case of the non staggered model, the fluid only passes through one channel as is presented in Figure 2.9.

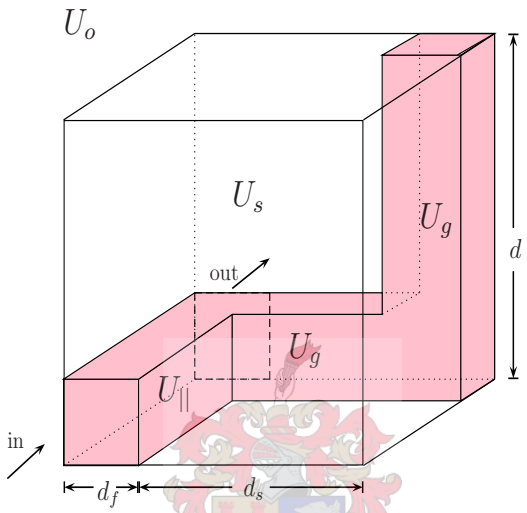

Figure 2.9: RRUC for the non-staggered foam model.

By applying equations (2.74) and (2.75) the hydrodynamic permeability and dimensionless hydrodynamic permeability for the non-staggered case can be written as a function of ϵ and ψ as follows,

$$k = \frac{\epsilon^2 d^2}{12\psi^2(\psi - 1)} \tag{2.80}$$

and hence,

$$K = \frac{\epsilon^2}{12\psi^2(\psi - 1)}. \tag{2.81}$$

In Figure 2.10 the non-dimensional permeabilities for the three levels of staggering are shown.

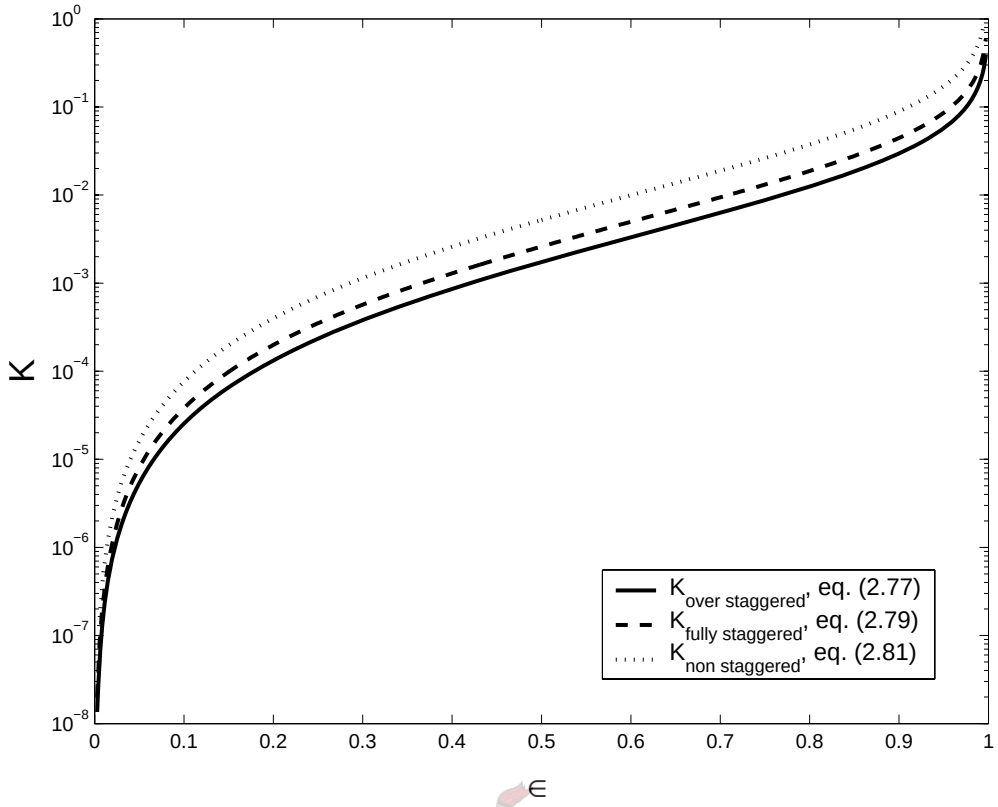

Figure 2.10: Dimensionless hydrodynamic permeability according to equations (2.77), (2.79) and (2.81).

It is evident from Figure 2.10 that the permeability for any particular ϵ decreases with staggering as is expected since an increase in staggering causes an increase in shear stress and thus renders the foam less permeable.

2.5.7 Modelling of inertial terms

For the Forchheimer regime inertial drag effects predominate. According to Du Plessis et al. (1994) the viscous shear stresses become insignificant in comparison to the form drag allowing equation (2.16) to be rewritten as,

$$-\epsilon\nabla\langle p\rangle_f = \frac{1}{\mathcal{U}_o}\iint_{S_{fs}} \underline{n}\, p\, dS. \tag{2.82}$$

If the weighing procedure of Section 2.5.5 is applied, equation (2.82) becomes,

$$-\epsilon\nabla\langle p\rangle_f = \underline{\frac{d_s}{d}\frac{1}{U_o}\iint_{S_{AA}} \underline{n}\, p\, dS} + \frac{d-d_s}{d}\frac{1}{U_o}\iint_{S_{BB}} \underline{n}\, p\, dS. \tag{2.83}$$

Figure 2.11 serves as a schematic for the evaluation of the surface integrals.

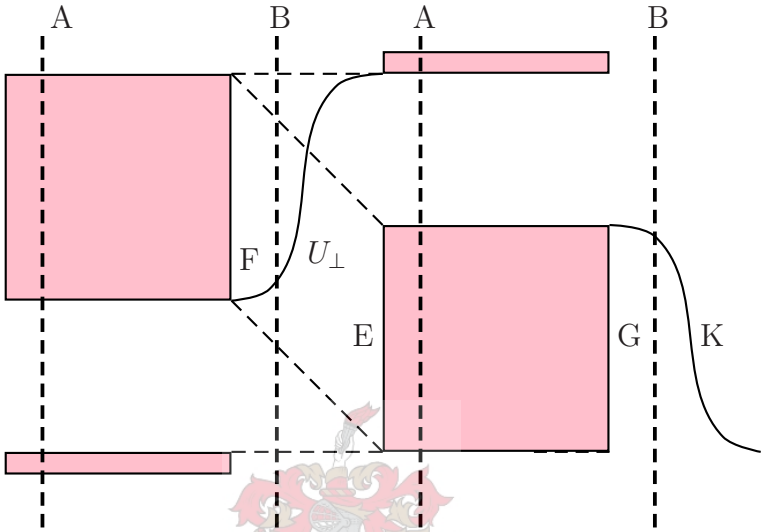

Figure 2.11: Schematic for the evaluation of surface integrals.

Assuming that the pressures exerted on walls E and F of Figure 2.11 are equal, the underlined term of equation (2.83) equals zero,

$$-\epsilon\nabla\langle p\rangle_f = \frac{d-d_s}{d}\frac{1}{U_o}\iint_{S_{BB}} \underline{n}\, p\, dS. \tag{2.84}$$

Under the assumption that the pressures on the transverse faces are constant, addition would result in a constant pressure difference, Δp, allowing equation (2.84) to be expressed as,

$$-\epsilon\nabla\langle p\rangle_f = \frac{d_f}{d}\frac{1}{U_o}\Delta p S_{face}\,\underline{\widehat{n}}. \tag{2.85}$$

The pressure difference term in equation (2.85) can now be modelled by applying the Bernoulli equation. Although the Bernoulli equation in the form given here, is only

applicable to vorticity free flow, it is used only to obtain an approximate value for the pressure drop.

$$\frac{p_E}{\rho} + \frac{w_E^2}{2} = \frac{p_K}{\rho} + \frac{w_K^2}{2}. \tag{2.86}$$

The fluid velocity at face E is assumed to be approximately zero due to the momentum conversion from a streamwise to a transverse direction at the surface. The pressure at K is adjacent to section G where the pressure is constant in the absence of any fluid. We can therefore approximate equation (2.86) as,

$$\frac{p_E}{\rho} = \frac{p_G}{\rho} + \frac{w_K^2}{2}. \tag{2.87}$$

This results in:

$$p_E - p_G = \frac{1}{2}\rho w_K^2. \tag{2.88}$$

For an average channel velocity of w, the pressure drop over the lee side of the circulation area can be expressed as

$$-\epsilon \nabla \langle p \rangle_f = \frac{d_f}{d}\frac{1}{U_o} c_d S_{face} \frac{1}{2}\rho w^2. \tag{2.89}$$

Here c_d constitutes a drag coefficient and S_{face} is the surface exposed upstream. Applying the relationship between q and w given in equation (2.51), results in the following:

$$-\epsilon \nabla \langle p \rangle_f = \frac{d_f}{d}\frac{1}{U_o} c_d S_{face} \frac{1}{2}\rho \frac{q^2\psi^2}{\epsilon^2}. \tag{2.90}$$

For the over-staggered case,

$$S_{face} = \frac{1}{2}d^2(\psi - 1)(3 - \psi) \tag{2.91}$$

and

$$\frac{\psi}{\epsilon} = \frac{4}{(3-\psi)^2}. \tag{2.92}$$

Substituting equations (2.91) and (2.92) into equation (2.90) results in the following:

$$\nabla \langle p \rangle_f = \frac{c_d \rho q^2}{2d} \frac{\psi(\psi - 1)}{\epsilon^3}. \tag{2.93}$$

The passability for the over-staggered case can thus be written as

$$\eta \equiv \frac{\rho q^2}{|\nabla \langle p \rangle_f|} = \frac{2d\epsilon^3}{(\psi - 1)\psi c_d}. \tag{2.94}$$

2.5.8 Derivation of a general momentum transport equation

From the definitions of permeability and passability, the pressure gradient for the viscous and inertial regimes is respectively given by,

$$\left.\frac{dp}{dx}\right|_{Re \to 0} \equiv \frac{\mu q}{k} \tag{2.95}$$

and

$$\left.\frac{dp}{dx}\right|_{Re >> 10} \equiv \frac{\rho q^2}{\eta} \tag{2.96}$$

The asymptotic matching technique developed by Churchill & Usagi (1972) is applied in order for a general momentum transport equation to be obtained. That is: an equation able to predict not only the limit scenarios, but also the intermediate conditions. Equation (2.95) is rewritten

$$\frac{dp}{dx} = G_o \mu q \tag{2.97}$$

where $G_o = \frac{1}{k}$. Equation (2.96) is rewritten as

$$\frac{dp}{dx} = G_\infty \mu q \tag{2.98}$$

where $G_\infty = \frac{\rho q}{\eta \mu}$. Let

$$G = (G_o^s + G_\infty^s)^{\frac{1}{s}}. \tag{2.99}$$

A general equation for momentum transport can then be written as

$$\frac{dp}{dx} = G\mu\,\underline{q}. \tag{2.100}$$

For the over-staggered case with, $s = 1$, the above can be written as,

$$\frac{dp}{dx} = \left(\frac{36\psi^2(\psi-1)}{\epsilon^2 d^2} + \frac{c_d\rho q}{\mu}\frac{\psi(\psi-1)}{2d\epsilon^3}\right)\mu\,\underline{q}. \tag{2.101}$$

Since the characteristic length d is unknown, equation (2.101) is written as,

$$\frac{1}{K} = \frac{36\psi^2(\psi-1)}{\epsilon^2} + \frac{c_d\psi(\psi-1)}{2\epsilon^3}Re_{qd}, \tag{2.102}$$

where Re_{qd} is defined as

$$Re_{qd} = \frac{\rho q d}{\mu}. \tag{2.103}$$

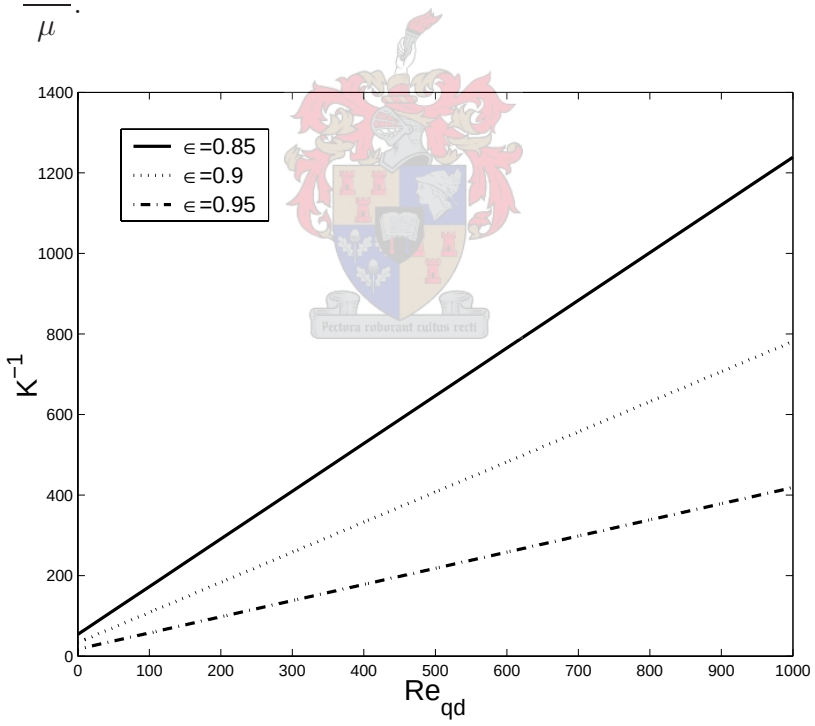

Figure 2.12: Equation (2.102) for 3 different porosities and $c_d = 2$.

Equation (2.102) is depicted in Figure 2.12 for a drag coefficient, $c_d = 2$, and porosities, $\epsilon = 0.85,\ 0.90,\ 0.95$.

2.5.9 Kozeny constant for the RUC model

The Kozeny constant, k_{oz}, is defined by Happel (1959) as

$$k_{oz} = \frac{\epsilon m^2}{k}, \tag{2.104}$$

where m is the hydraulic radius, defined for a porous medium as

$$m = \frac{\text{free volume}}{\text{wetted area}}. \tag{2.105}$$

In the present case, the hydraulic radius for the RUC model is, $m = \frac{U_f}{S_{fs}}$, and the Kozeny constant may therefore be expressed as

$$k_{oz} = \frac{d^2\epsilon^3}{9K(\psi^2 - 4\psi + 3)}. \tag{2.106}$$

The value for k_{oz} is determined for all three RUC models. For the over-staggered model it is,

$$\frac{4\,\epsilon\,\psi^2}{(-3+\psi)^2\,(-1+\psi)}. \tag{2.107}$$

For the fully staggered and non-staggered model it is respectively,

$$\frac{8\,\epsilon\,\psi^2}{3\,(-3+\psi)^2\,(-1+\psi)} \tag{2.108}$$

and

$$\frac{4\,\epsilon\,\psi^2}{3\,(-3+\psi)^2\,(-1+\psi)}. \tag{2.109}$$

The Kozeny constant is determined at different porosities for each model and shown in Table 2.1.

Table 2.1: Kozeny Constant (k_{oz}) for the RUC model.

porosity	over-staggered model eq. (2.107)	fully staggered model eq. (2.108)	non-staggered model eq. (2.109)
0.9900	11.8558	7.9039	3.9519
0.9500	7.5795	5.0530	2.5265
0.9000	6.8818	4.5879	2.2939
0.8000	6.7939	4.5293	2.2646
0.7000	7.0838	4.7225	2.3613
0.6000	7.5022	5.0015	2.5007
0.5000	8.0000	5.3333	2.6667
0.4000	8.5704	5.7136	2.8568

2.5.10 Application to non-Newtonian purely viscous flow

This section is a synopsis of work done by Smit et al. (2005), attached as Appendix D. Smit et al. (2005) states that the shear stress for a power-law fluid is given by

$$\tau_w = C\left(\frac{2n+1}{n}\right)^n \left(\frac{\chi}{\epsilon}\right)^n \left(\frac{2q}{(d-d_s)}\right)^n. \tag{2.110}$$

where C is the absolute viscosity for a power-law fluid and n is a power-law constant. The tortuosity, χ, is given by

$$\frac{\chi}{\epsilon} = \frac{4}{(3-\chi)^2}. \tag{2.111}$$

For the over-staggered model, $\psi = \chi$, and equation (2.110) can be expressed as

$$\tau_w = C\left(\frac{2n+1}{n}\right)^n \left(\frac{4}{(3-\psi)^2}\right)^n \left(\frac{2q}{(d-d_s)}\right)^n. \tag{2.112}$$

In chapter 2, equation (2.70), the pressure gradient was expressed as follows

$$-\nabla\langle p\rangle = \frac{U_f}{U_{||}+U_t}\cdot\frac{S_{||}+\beta S_\perp}{U_o}\tau_w\,\underline{\hat{n}}. \tag{2.113}$$

By substituting the expression for the wall-shear stress, equation (2.112), into equation (2.113), the pressure gradient for power-law creep flow may then be written as

$$-\frac{dp_f}{dx} = \frac{S_{||} + \beta S_{\perp}}{\epsilon U_o} C \left(\frac{2n+1}{n}\right)^n \left(\frac{U_f}{U_{||} + U_t}\right)^{n+1} \left(\frac{2q}{d_f \epsilon}\right)^n. \tag{2.114}$$

By substituting the geometrical parameters of the over-staggered model, (Smit et al. (2005)), into equation (2.114), the intrinsic phase average pressure may then be expressed as,

$$-\frac{dp_f}{dx} = \frac{2^{4n+2} 3(\psi - 1)}{d^{n+1}(3-\psi)^{3n+1}} \left(\frac{2n+1}{n}\right)^n C q^n. \tag{2.115}$$

Smit et al. (2005) showed that equation (2.115), compares favourably with experimental data supplied by Sabiri, 1995.

Chapter 3

Viscous flow relative to arrays of cylinders

The model, developed in Chapter 2, is based on results for flow between parallel plates. This configuration seems feasible for foamlike media at low porosities. Metallic foams, however, normally have porosities well above 95%, yielding the parallel plate-model less plausible. In the search of a more appropriate 'flow by' model this chapter is devoted to appropriate work in this field.

Happel & Brenner (1983) reported on flow relative to groups of cylindrical objects in cases of high porosity. As is shown in Figure 3.1, two concentric cylinders serve as a model for fluid moving through an assemblage of cylinders.

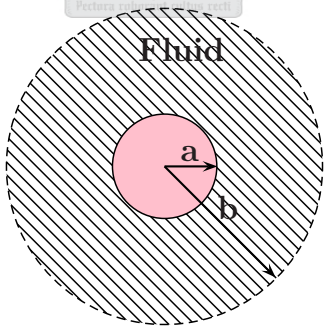

Figure 3.1: Free surface model for flow relative to a cylinder in a cylindrical duct.

The inner cylinder, of radius a, resembles one of the rods in the assemblage and the outer cylinder, of radius b, a fluid envelope with a free surface. The porosity of the model is assumed to be the same as that of the assemblage. It is also assumed that the exact

shape of the outside boundary has little influence on the flow velocity due to the high porosity–typically above 95%. A boundary condition of no slippage along the walls of the fluid envelope must be maintained.

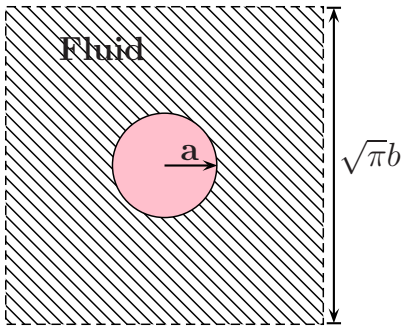

Figure 3.2: Model for flow relative to a cylinder in a square duct with frictionless outer boundary.

Figure 3.2 shows the unit cell in a square array as compared to the model for axial flow. The cross hatched area occupied by fluid is the same for both the array and the model. The dotted line indicates the outside frictionless boundary of the fluid envelope.

The use of this model and the application of appropriate boundary conditions facilitate the closure of solutions to the volume averaged Navier Stokes equation. Flow is firstly assumed to be parallel and secondly to be perpendicular to a single cylinder. These results can then be applied to a random assemblage of cylinders by giving twice the weight to perpendicular flow as for flow parallel to cylinders. These ratios are due to the fact that the cylinder can be in a horizontal or vertical position when flow is perpendicular to it, but there is only one position for which flow will be parallel to it.

3.1 Flow parallel to the cylinders

In the following analysis the original notation, as used by Happel & Brenner (1983), will be followed to facilitate comparison. The fluid is moving through the annular space between the cylinder of radius, a, and the fluid envelope of radius, b. The differential equation to be solved is

$$\frac{\partial P}{\partial x} = \frac{\mu}{r}\frac{d}{dr}\left(r\frac{du}{dr}\right). \tag{3.1}$$

Here u denotes the fluid velocity in the axial, x, direction. The solution to this equation, for constant $\frac{dp}{dx}$, is given by

$$u = \frac{1}{4\mu}\frac{dp}{dx}r^2 + A\ln r + B. \tag{3.2}$$

The boundary conditions are:

$$u = 0 \quad \text{at} \quad r = a \tag{3.3}$$

$$\frac{du}{dr} = 0 \quad \text{at} \quad r = b. \tag{3.4}$$

The complete solution to equation (3.1) is then given by

$$u = -\frac{1}{4\mu}\frac{dp}{dx}\left[(a^2 - r^2) + 2b^2\ln\frac{r}{a}\right]. \tag{3.5}$$

The flow rate is determined as

$$Q = 2\pi\int_a^b ur\,dr = \frac{-\pi}{8\mu}\frac{dp}{dx}\left[4a^2b^2 - a^4 - 3b^4 + 4b^4\ln\frac{b}{a}\right]. \tag{3.6}$$

The Darcy velocity is given by $q = \frac{Q}{\pi b^2}$,

$$q = \frac{\frac{dp}{dx}\left(a^4 - 4\,a^2\,b^2 + 3\,b^4 - 4\,b^4\,\ln(\frac{b}{a})\right)}{8\,b^2\,\mu}. \tag{3.7}$$

The pressure gradient in terms of q is thus given as follows,

$$\frac{dp}{dx} = \frac{8\,b^2\,\mu\,q}{a^4 - 4\,a^2\,b^2 + 3\,b^4 - 4\,b^4\,\ln(\frac{b}{a})}. \tag{3.8}$$

The resulting drag per unit length on the cylinder is thus given by,

$$f_{||} = \frac{dp}{dx}\pi(b^2 - a^2) = \frac{8\,b^2\,(-a^2 + b^2)\,\mu\,\pi\,q}{a^4 - 4\,a^2\,b^2 + 3\,b^4 - 4\,b^4\,\log(\frac{b}{a})} \tag{3.9}$$

and the total drag in an RUC of side length, d, in the flow direction is thus given by,

$$F_{||} = f_{||}d = \frac{8\,b^2\,(-a^2 + b^2)\,d\,\mu\,\pi\,q}{a^4 - 4\,a^2\,b^2 + 3\,b^4 - 4\,b^4\,\log(\frac{b}{a})}. \tag{3.10}$$

3.2 Flow perpendicular to the cylinders

In order to describe the flow of fluid perpendicular to the inner cylinder we turn to the Navier-Stokes and continuity equations, respectively given by Hughes & Gaylord (1964) as

$$\begin{aligned}\rho\frac{D\,\underline{v}}{Dt} &= -\nabla p+\mu\nabla^2\,\underline{v}+1/3\mu\nabla(\nabla\cdot\,\underline{v})+2(\nabla\mu)\cdot\nabla\,\underline{v}+(\nabla\mu)\times(\nabla\times\,\underline{v})\\ &\quad -\frac{2}{3}(\nabla\mu)(\nabla\cdot\,\underline{v})+\kappa\nabla(\nabla\cdot\,\underline{v})+(\nabla\kappa)(\nabla\cdot\,\underline{v})+\rho\,\underline{F}\end{aligned} \tag{3.11}$$

and

$$\frac{\partial\rho}{\partial t} = -\nabla\cdot(\rho\,\underline{v}). \tag{3.12}$$

For the purposes of this work, certain assumptions are to be made. Firstly the fluid is assumed to be incompressible, ρ is therefore constant and the equation of continuity reduces to

$$\nabla\cdot\,\underline{v} = 0. \tag{3.13}$$

Secondly, it is assumed that only fluids with constant viscosity is taken into consideration which simplifies equation (3.11) even further since, $\nabla\mu = 0$. Subsequent application of these two assumptions renders,

$$\rho\frac{D\,\underline{v}}{Dt} = -\nabla p+\mu\nabla^2\,\underline{v}+\rho\,\underline{F}. \tag{3.14}$$

In all the above the operator, $\frac{D}{Dt}$, is the time derivative along a path following the fluid motion. Commonly known as the Stokes operator or the substantial derivative, $\frac{D}{Dt}$, is defined as follows:

$$\frac{D}{Dt} = \frac{\partial}{\partial t}+\underline{v}\cdot\nabla. \tag{3.15}$$

Equation (3.14) now becomes

$$\rho\frac{\partial\,\underline{v}}{\partial t}+\rho\,\underline{v}\cdot\nabla\,\underline{v} = -\nabla p+\mu\nabla^2\,\underline{v}+\rho\,\underline{F}. \tag{3.16}$$

It is assumed that the flow under consideration is time independent and that the non-linear inertial terms (i.e. $\underline{v}\cdot\nabla\,\underline{v}$) can be dropped. For the time being the latter assumption

is quite acceptable since in the low Reynolds number limit (Re $\longrightarrow$0) only viscous drag is present. If the body force, $\underline{F}$, is negligible the original Navier-Stokes equation and the equation of continuity for the above mentioned conditions is given by,

$$0 = -\nabla p + \mu \nabla^2 \underline{v} \tag{3.17}$$

and

$$\nabla \cdot \underline{v} = 0, \tag{3.18}$$

respectively. Since, in this section, we are considering cylinders, the vector equations (3.17) and (3.18) are to be written in cylindrical coordinates. For this transformation it is necessary to recap a few basics. The derivative of cylindrical unit vectors, $\underline{e}_r$ and $\underline{e}_\theta$, with θ, is given by

$$\frac{\partial \underline{e}_r}{\partial \theta} = -\underline{e}_\theta \tag{3.19}$$

and

$$\frac{\partial \underline{e}_\theta}{\partial \theta} = \underline{e}_r. \tag{3.20}$$

From the definition of the del operator, the laplace operator, ∇^2, may be written in two dimensional cylindrical coordinates as,

$$\nabla^2 = \frac{\partial^2}{\partial r^2} + \frac{1}{r}\frac{\partial}{\partial r} + \frac{1}{r^2}\frac{\partial^2}{\partial \theta^2}. \tag{3.21}$$

The Navier-Stokes equation is then given by,

$$\begin{aligned} 0 = & -\left(\frac{\partial p}{\partial r}\underline{e}_r + \frac{1}{r}\frac{\partial p}{\partial \theta}\underline{e}_\theta\right) \\ & +\mu\left(\frac{\partial^2 (v\underline{e}_r + v\underline{e}_\theta)}{\partial r^2} + \frac{1}{r}\frac{\partial (v\underline{e}_r + v\underline{e}_\theta)}{\partial r} + \frac{1}{r^2}\frac{\partial^2 (v\underline{e}_r + v\underline{e}_\theta)}{\partial \theta^2}\right). \end{aligned} \tag{3.22}$$

and the continuity equation by,

$$\frac{\partial v_r}{\partial r} + \frac{v_r}{r} + \frac{1}{r}\frac{\partial v_\theta}{\partial \theta} = 0. \tag{3.23}$$

Subsequent application of equations (3.19) and (3.20) to equation (3.22) then yields the following radial and transverse components

$$\frac{\partial p}{\partial r} = \mu\left(\nabla^2 v_r - \frac{v_r}{r^2} - \frac{2}{r^2}\frac{\partial v_\theta}{\partial \theta}\right) \tag{3.24}$$

and

$$\frac{1}{r}\frac{\partial p}{\partial \theta} = \mu\left(\nabla^2 v_\theta - \frac{v_\theta}{r^2} + \frac{2}{r^2}\frac{\partial v_r}{\partial \theta}\right). \tag{3.25}$$

The stream function is given by Happel (1959) as,

$$\psi = \left(\frac{F}{r} + E\,r + \frac{C\,r^3}{8} + \frac{D\,r\,\left(-\frac{1}{2} + \log r\right)}{2}\right)\sin\theta \tag{3.26}$$

where

$$\begin{aligned} C &= \frac{-8\,a^2\,q}{-a^4 + b^4 + 2\,(a^4 + b^4)\,\log(\frac{a}{b})} \\ D &= \frac{4\,(a^4 + b^4)\,q}{-a^4 + b^4 + 2\,(a^4 + b^4)\,\log(\frac{a}{b})} \\ E &= \frac{(a^4 + b^4)\,q\,(1 - 2\,\log a)}{-a^4 + b^4 + 2\,(a^4 + b^4)\,\log(\frac{a}{b})} \\ F &= \frac{a^2\,b^4\,q}{-a^4 + b^4 + 2\,(a^4 + b^4)\,\log(\frac{a}{b})}. \end{aligned} \tag{3.27}$$

In cylindrical coordinates the axial stream function is defined by the relations

$$v_r = \frac{1}{r}\frac{\partial \psi}{\partial \theta} \text{ and } v_\theta = -\frac{\partial \psi}{\partial r}. \tag{3.28}$$

Implementing equation (3.26) yields

$$v_r = \frac{q\,\cos\theta\,\left(a^2\,\left(b^4 - r^4\right) + 2\,\left(a^4 + b^4\right)\,r^2\,\left(-\log a + \log(r)\right)\right)}{r^2\,\left(-a^4 + b^4 + 2\,\left(a^4 + b^4\right)\,\log(\frac{a}{b})\right)} \tag{3.29}$$

and

$$v_\theta = \frac{q\,\left(a^2\,b^4 - 2\,\left(a^4 + b^4\right)\,r^2 + 3\,a^2\,r^4 + 2\,\left(a^4 + b^4\right)\,r^2\,\left(\log(\frac{b}{r})\right)\right)\,\sin\theta}{r^2\,\left(-a^4 + b^4 + 2\,\left(a^4 + b^4\right)\,\log(\frac{a}{b})\right)}. \tag{3.30}$$

The viscous stresses are given by

$$\tau_{rr} = 2\mu\left(\frac{\partial v_r}{\partial r}\right) \tag{3.31}$$

and

$$\tau_{r\theta} = \mu\left[r\frac{\partial}{\partial r}\left(\frac{v_\theta}{r}\right) + \frac{1}{r}\frac{\partial v_r}{\partial \theta}\right]. \tag{3.32}$$

Replacing v_r and v_θ with equations (3.29) and (3.30), yields

$$\tau_{rr} = \frac{4\,\mu\,(a^2 - r^2)\,(-b^4 + a^2\,r^2)\,q\,\cos\theta}{r^3\left(-a^4 + b^4 + 2\,(a^4 + b^4)\,\log(\frac{a}{b})\right)} \tag{3.33}$$

and

$$\tau_{r\theta} = \frac{4\,a^2\,\mu\,(-b^4 + r^4)\,q\,\sin\theta}{r^3\left(-a^4 + b^4 + 2\,(a^4 + b^4)\,\log(\frac{a}{b})\right)}. \tag{3.34}$$

The stress dyad for the fluid passing over the inner cylinder, radius a, is given by

$$\underline{\underline{\sigma}} = -p\underline{\underline{1}} + \underline{\underline{\tau}} = -p_{rr} + \tau_{rr} + \tau_{r\theta} \tag{3.35}$$

and its components are shown in Figure 3.3.

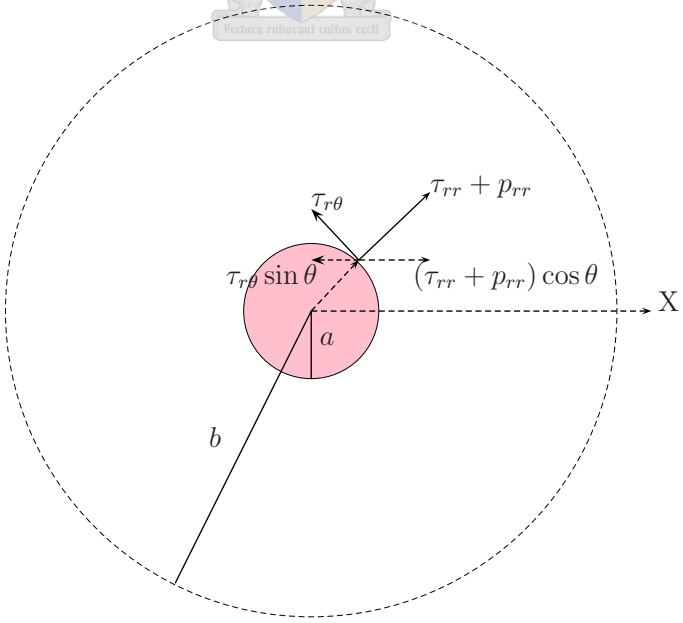

Figure 3.3: Components of the stress diadic.

Equations (3.24) and (3.25) are integrated and the pressure term is determined as,

$$p = \frac{-4\,\mu\,(a^4+b^4+2\,a^2\,r^2)\;q\,\cos\theta}{r\left(-a^4+b^4+2\,(a^4+b^4)\,\log(\frac{a}{b})\right)}. \tag{3.36}$$

The streamwise-component of the stress dyad is given by

$$\sigma_{xx} = (-p_{rr}+\tau_{rr})\cos\theta - \tau_{r\theta}\sin\theta. \tag{3.37}$$

The drag force in the x-direction on the inner cylinder is therefore given by,

$$W = \int_0^{2\pi}\sigma_{xx}d\,\theta = \frac{-8\,(a^4+b^4)\,\mu\,\pi\,q}{-a^4+b^4+2\,(a^4+b^4)\,\log(\frac{a}{b})}. \tag{3.38}$$

Written in terms of the constant, D, in equation (3.26), the above yields

$$W = 2\pi\mu D. \tag{3.39}$$

The drag per unit length for perpendicular fluid motion is therefore given by,

$$f_\perp = \frac{4\,\mu\,\pi\,q}{\frac{-(-a^4+b^4)}{2\,(a^4+b^4)}+\log(\frac{b}{a})} \tag{3.40}$$

and the drag in an RUC of side length d is,

$$F_\perp = f_\perp d = \frac{4\,d\,\mu\,\pi\,q}{\frac{-(-a^4+b^4)}{2\,(a^4+b^4)}+\log(\frac{b}{a})}. \tag{3.41}$$

3.3 Total drag on cylinders in an RUC

The total drag experienced by fluid moving through an RUC is assumed to be the sum of the drags on the three cylinders constituting the RUC, of which one is orientated streamwise and the other two transverse. We then define

$$\mathcal{F} = \left(F_{||}+2F_\perp\right) = 8\,d\,\mu\,\pi\,q\left(\frac{1}{\frac{a^4-b^4}{2(a^4+b^4)}+\log(\frac{b}{a})}+\frac{b^2\,(-a^2+b^2)}{a^4-4\,a^2\,b^2+3\,b^4-4\,b^4\,\log(\frac{b}{a})}\right). \tag{3.42}$$

The pressure gradient can be written as

$$\frac{d\langle p\rangle_f}{dx} = \frac{\Delta\langle p\rangle_f}{\Delta x}. \tag{3.43}$$

Each cell has a side length, d, therefore we have:

$$\frac{d\langle p\rangle_f}{dx} = \frac{\langle p_2\rangle_f - \langle p_1\rangle_f}{d}. \tag{3.44}$$

Since the pressure on each of the cell borders is assumed constant, the average of the fluid pressure is equal to the pressure at any point in the fluid, on the border, therefore

$$\langle p\rangle_f = p \tag{3.45}$$

and we have

$$\frac{d\langle p\rangle_f}{dx} = \frac{p_2 - p_1}{d}. \tag{3.46}$$

Subsequent application of the definition of pressure as force per unit area, results in

$$-\frac{d\langle p\rangle_f}{dx} = \frac{\mathcal{F}}{d\pi(b^2 - a^2)}. \tag{3.47}$$

Here $\mathcal{F}$ is the net frictional force exerted by a cylinder of length, d, on the bypassing fluid. The friction factor, denoted by F, is defined as

$$F \equiv \frac{1}{k}. \tag{3.48}$$

Application of the definition of permeability results in

$$F = \frac{-\frac{dp}{dx}}{\mu q}. \tag{3.49}$$

Substitution of equation (3.47) into equation (3.49) yields,

$$F = \frac{\mathcal{F}}{\mu q d\pi(b^2 - a^2)}. \tag{3.50}$$

Subsequently, from equation (3.42) we have,

$$F = \frac{8\left(\frac{1}{\frac{a^4-b^4}{2\left(a^4+b^4\right)}+\log\left(\frac{b}{a}\right)}+\frac{b^2\left(-a^2+b^2\right)}{a^4-4\,a^2\,b^2+3\,b^4-4\,b^4\,\log\left(\frac{b}{a}\right)}\right)}{-a^2+b^2}. \tag{3.51}$$

3.4 Comparison between the RUC and cylindrical models

The corresponding surface areas of the two models are equated as

$$\pi a^2 = d_s^2 \tag{3.52}$$

for the cross-sectional strand area and

$$\pi b^2 = d^2 \tag{3.53}$$

for the lateral unit cell area. The volume of the solid material in the RUC is given as

$$U_s = 3\,d\,{d_s}^2 - 2\,{d_s}^3. \tag{3.54}$$

The porosity is defined as,

$$\epsilon = \frac{U_f}{U_o} = 1 - \frac{U_s}{U_o}. \tag{3.55}$$

Substitution of equation (3.54) into equation (3.55) renders

$$\epsilon = 1 - \frac{3\,{d_s}^2}{d^2} + \frac{2\,{d_s}^3}{d^3}. \tag{3.56}$$

The following expression is then obtained for d_s

$$\frac{d_s}{d} = \frac{2+\frac{1-i\sqrt{3}}{\left(1+2\sqrt{-1+\epsilon}\,\sqrt{\epsilon}-2\,\epsilon\right)^{\frac{1}{3}}}+\left(1+i\sqrt{3}\right)\left(1+2\sqrt{-1+\epsilon}\,\sqrt{\epsilon}-2\,\epsilon\right)^{\frac{1}{3}}}{4}. \tag{3.57}$$

An expression for d_s is obtained from equation (3.57) which is then combined with equation (3.52) to obtain the following expression for the inner radius of the cylindrical model.

$$a = \frac{d\left(2+\frac{1-i\sqrt{3}}{\left(1+2\sqrt{-1+\epsilon}\sqrt{\epsilon}-2\epsilon\right)^{\frac{1}{3}}}+\left(1+i\sqrt{3}\right)\left(1+2\sqrt{-1+\epsilon}\sqrt{\epsilon}-2\epsilon\right)^{\frac{1}{3}}\right)}{4\sqrt{\pi}}. \quad (3.58)$$

The graphs for $\frac{a}{d}$ and $\frac{d_s}{d}$ against porosity are shown in Figure 3.4. The discrepancy

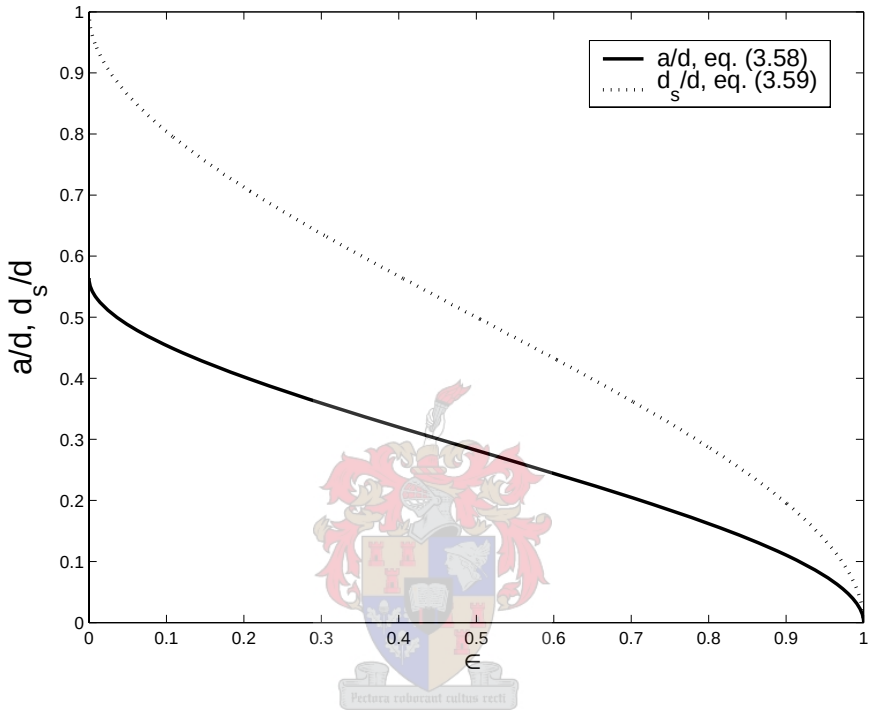

Figure 3.4: $\frac{a}{d}$ and $\frac{d_s}{d}$ as functions of porosity.

between the two models is due to the fact that

$$\frac{d_s}{d} = \sqrt{\pi}\frac{a}{d} \quad (3.59)$$

and the models will thus always differ with a ratio of $\sqrt{\pi}$. In previous work the following expression for the dimensionless friction factor, in terms of radii a and b, was obtained

$$F = \frac{8\,d^2\left(\frac{1}{\frac{a^4-b^4}{2\left(a^4+b^4\right)}+\log\left(\frac{b}{a}\right)}+\frac{b^2\left(-a^2+b^2\right)}{a^4-4\,a^2\,b^2+3\,b^4\,\log\left(\frac{b}{a}\right)}\right)}{-a^2+b^2}. \quad (3.60)$$

Equations (3.58) and (3.53) are substituted into the equation (3.60) rendering the following expression for the friction factor in terms of RUC-parameters.

$$F = \frac{128\,\pi\left(\frac{1}{\frac{-256+S^4}{2\,(256+S^4)}+\log(\frac{4}{S})}+\frac{16\,(16-S^2)}{-64\,S^2+S^4+768\,\log(\frac{4}{S})}\right)}{16-S^2}, \tag{3.61}$$

where

$$\begin{aligned} S &= 2+\frac{1-i\,\sqrt{3}}{\left(1+2\,\sqrt{-1+\epsilon}\,\sqrt{\epsilon}-2\,\epsilon\right)^{\frac{1}{3}}} \\ &\quad +\left(1+i\,\sqrt{3}\right)\,\left(1+2\,\sqrt{-1+\epsilon}\,\sqrt{\epsilon}-2\,\epsilon\right)^{\frac{1}{3}}. \end{aligned} \tag{3.62}$$

The dimensionless friction factor is defined as

$$F \equiv \frac{1}{K}. \tag{3.63}$$

The dimensionless permeability of the cylindrical model thus is,

$$K_c = \frac{1}{F} \tag{3.64}$$

where F is given by equation (3.61). The dimensionless permeability of the cylindrical model is compared to that of the original RUC in Figure 3.5.

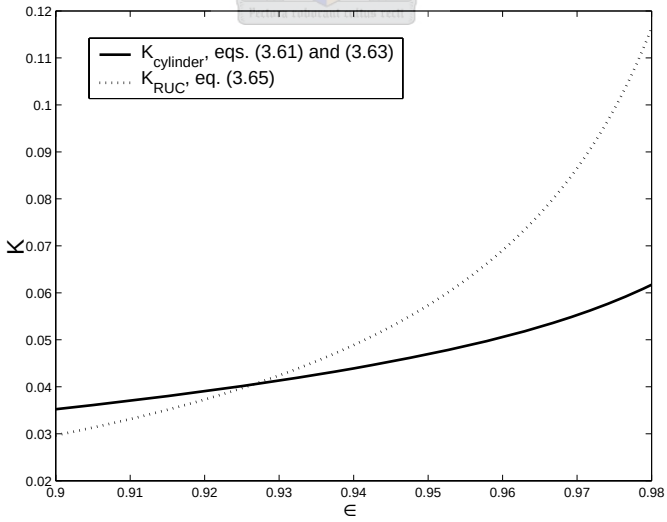

Figure 3.5: Comparison between the permeability predictions of the cylindrical- and the RUC–model, (equations (3.64) and (3.65)).

Here the dimensionless permeability for the original RUC model is

$$K = \frac{\epsilon^2}{36\psi^2(\psi-1)} \tag{3.65}$$

and

$$\psi = 2 + 2\cos\left[\frac{4\pi + \arccos(2\epsilon - 1)}{3}\right]. \tag{3.66}$$

The relation between the d-values for the RUC and the cylindrical model can be obtained by determining the ratio-relation between their respective friction factors, F_C and F_R:

$$\frac{d_c}{d_r} = \sqrt{\frac{F_C}{F_R}}. \tag{3.67}$$

The expression obtained for d_c is then denoted by

$$d_c = \frac{4\,d\,\sqrt{2\,\pi}\,\sqrt{\dfrac{\epsilon^2\left(\frac{1}{\frac{-256+G^4}{2\,(256+G^4)}+\log(\frac{4}{G})}+\frac{16\,(16-G^2)}{-64\,G^2+G^4+768\,\log(\frac{4}{G})}\right)}{(16-G^2)\,\psi^2\left(1+2\,\cos(\frac{4\,\pi+\arccos(-1+2\,\epsilon)}{3})\right)}}}{3} \tag{3.68}$$

where the expressions for G and ψ are

$$G = 2 + \frac{1-i\,\sqrt{3}}{\left(1+2\,\sqrt{-1+\epsilon}\,\sqrt{\epsilon}-2\,\epsilon\right)^{\frac{1}{3}}} + \left(1+i\,\sqrt{3}\right)\left(1+2\,\sqrt{-1+\epsilon}\,\sqrt{\epsilon}-2\,\epsilon\right)^{\frac{1}{3}}$$

$$\psi = 2 + 2\,\cos(\frac{4\,\pi+\arccos(-1+2\,\epsilon)}{3}). \tag{3.69}$$

The cylindrical model is only valid for Newtonian flow, since this assumption was made in determining the drag on the cylinders for perpendicular flow. The RUC on the other hand may be generalised for the case of non-Newtonian flow. In this work, the RUC model has been modified allowing it to predict the permeability for both the Darcy and the Forchheimer regime. The cylindrical model is also only valid for slow flow and generalisation towards the inertial regime may prove extremely difficulty if not impossible.

3.5 The Kozeny constant for different cell models

The Kozeny constant, k_{oz}, was defined by Carman (1956) as:

$$k_{oz} \equiv \frac{\epsilon m^2}{K}. \tag{3.70}$$

It can be rewritten in terms of the friction factor as

$$k_{oz} = F\epsilon m^2 \tag{3.71}$$

and was intended to be a constant value for all porous media. Equations (3.72), (3.73) and (3.74) give the Kozeny constant for parallel, perpendicular and random orientation flow cell models respectively as was determined by Happel & Brenner (1983):

$$k_{oz||} = \frac{2\epsilon^3}{(1-\epsilon)[2\ln(1/(1-\epsilon)) - 3 + 4(1-\epsilon) - (1-\epsilon)^2]}, \tag{3.72}$$

$$k_{oz\perp} = \frac{2\epsilon^3}{(1-\epsilon)[\ln\{1/(1/\epsilon)\} - 1 - (1-\epsilon)^2/\{1+(1-\epsilon)^2\}]} \tag{3.73}$$

and

$$k_{oztot} = \frac{1}{3}k_{oz||} + \frac{2}{3}k_{oz\perp}. \tag{3.74}$$

These constants, evaluated for different fractional void volumes, are given in Tabel 3.1 and they are evidently not constant.

The solid-fluid interface, S_{fs}, for the cylindrical RUC model is determined as,

$$S_{fs} = 6\pi a(d_c - 2a). \tag{3.75}$$

Substituting equation (3.58) into the above and applying the definition of $m = \frac{U_f}{S_{fs}}$, and, $k_{oz} = \frac{\epsilon m^2}{k}$ renders the following expression for the Kozeny constant of the cylindrical RUC model,

$$k_{oz} = \frac{512\,\epsilon^3\left(\frac{1}{\frac{-256+(T+U)^4}{2\left(256+(T+U)^4\right)}+\log(\frac{4}{T+U})} + \frac{16\left(16-(T+U)^2\right)}{-64\,(T+U)^2+(T+U)^4+768\,\log(\frac{4}{T+U})}\right)}{9\,(T+U)^2\left(1-\frac{T+U}{2\sqrt{\pi}}\right)^2\left(16-(T+U)^2\right)} \tag{3.76}$$

where,

$$T = \frac{1-i\sqrt{3}}{\left(1+2\sqrt{-1+\epsilon}\,\sqrt{\epsilon}-2\,\epsilon\right)^{\frac{1}{3}}} \tag{3.77}$$

Table 3.1: Kozeny constant as predicted by different cell models.

Fractional Void Volume, ϵ	Flow Parallel to Cylinders, $k_{oz\|\|}$ eq. (3.72)	Flow Perpendicular to Cylinders, $k_{oz\perp}$ eq. (3.73)	Flow through Random Orientation of Cylinders, k_{oztot} eq. (3.74)
0.9900	31.0484	53.8252	46.2329
0.9000	7.3076	11.0255	9.7862
0.8000	5.2305	7.4596	6.7166
0.7000	4.4149	6.1951	5.6017
0.6000	3.9621	5.6205	5.0677
0.5000	3.6685	5.3678	4.8014
0.4000	3.4603	5.3019	4.6880

and

$$U = 2 + \left(1 + i\sqrt{3}\right)\left(1 + 2\sqrt{-1+\epsilon}\sqrt{\epsilon} - 2\epsilon\right)^{\frac{1}{3}}. \tag{3.78}$$

The Kozeny constants for the RUC model and that of the cylindrical model are compared to each other for adequately high values of ϵ in Table 3.2.

Table 3.2: Comparison between Kozeny constants for the RUC and the cylindrical model.

ϵ	Kozeny constant, k_{oz}	
	over-staggered RUC model eq. (2.107)	Cylindrical model eq. (3.76)
0.90	6.88	7.86
0.91	6.95	8.40
0.92	7.04	9.04
0.93	7.17	9.85
0.94	7.34	10.88
0.95	7.58	12.28
0.96	7.93	14.28

Chapter 4

Improved model and experimental results

The present model, as discussed in chapter 2, has since been adapted by Crosnier et al. (2006). An approach similar to that of Lloyd et al. (2004) for 2D structures is followed to model the inertial effects.

As previously discussed, the flow through a foam is governed by the following form of the averaged Navier-Stokes equation (2.16):

$$-\nabla\langle p\rangle = \frac{1}{U_o}\iint_{S_{fs}} \underline{n}\, p\, dS - \frac{1}{U_o}\iint_{S_{fs}} \mu\, \underline{n}\cdot\nabla\underline{v}\, dS. \tag{4.1}$$

Following Lloyd et al. (2004), the two integrals in equation (4.1) are split into streamwise and transverse integrals, yielding

$$\begin{aligned} -\nabla\langle p\rangle = {} & \underline{\frac{1}{U_o}\iint_{S_{\parallel}} \underline{n}\, p\, dS} + \frac{1}{U_o}\iint_{S_{\perp}} \underline{n}\, p\, dS \\ & \underline{- \frac{1}{U_o}\iint_{S_{\parallel}} \mu\, \underline{n}\cdot\nabla\,\underline{v}\, dS} - \underline{\frac{1}{U_o}\iint_{S_{\perp}} \mu\, \underline{n}\cdot\nabla\,\underline{v}\, dS} \end{aligned} \tag{4.2}$$

of which the underlined integrals are zero. In the remaining pressure integral, for each transverse channel section, the pressure is split into a channel wall average pressure, $\overline{p_w}$, and a wall pressure deviation, $\widetilde{p_w}$, yielding,

$$-\nabla\langle p\rangle = \frac{1}{U_o}\iint_{S_{\perp}} \underline{n}\,\overline{p_w}\, dS + \frac{1}{U_o}\iint_{S_{\perp}} \underline{n}\,\widetilde{p_w}\, dS - \frac{1}{U_o}\iint_{S_{\parallel}} \mu\, \underline{n}\cdot\nabla\,\underline{v}\, dS. \tag{4.3}$$

In evaluating the perpendicular surface integrals, the integral over all possible RRUC's must be taken to comply with the notion that an RRUC is a proper substitute for an REV. Since the pressure equation at hand is streamwise, this will only effect integration over $S_\perp$ planes.

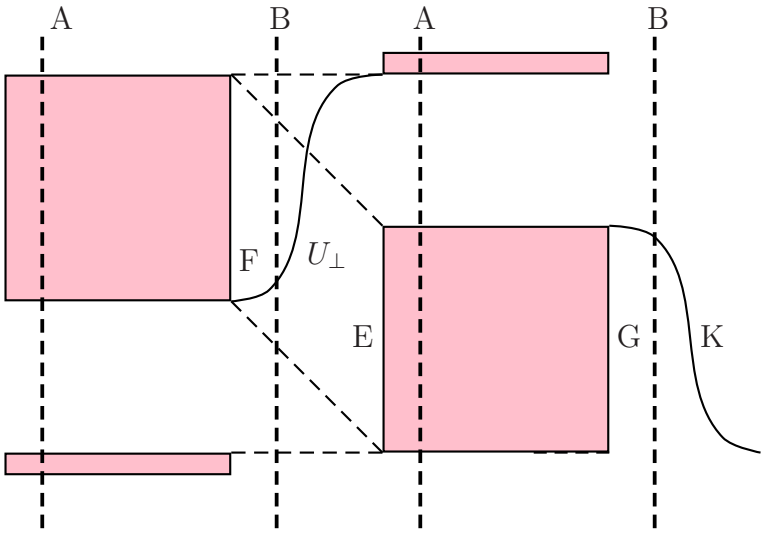

Figure 4.1: Schematic for the evaluation of surface integrals.

In Figure 4.1 is shown schematically the notation followed here. Let the integrals over S_{AA} and S_{BB} respectively denote an integral over a cell of which the walls cut through solid parts as shown by the dashed lines A, and a second integral where the cell walls do not cut though any solid as shown by the dashed lines B. The average wall pressure integrals need to be weighed according to their relative frequency of occurrence. This need not be done with the parallel surfaces or pressure deviation on perpendicular surfaces, since a shift in the streamwise direction does not result in any loss of friction. It follows that,

$$
\begin{aligned}
-\nabla\langle p\rangle \;=\; & \frac{d_s}{d}\cdot\frac{1}{U_o}\underset{S_{AA}}{\iint}\underline{n}\,\overline{p_w}\,dS \;+\; \frac{d-d_s}{d}\cdot\frac{1}{U_o}\underset{S_{BB}}{\iint}\underline{n}\,\overline{p_w}\,dS \\
& + \frac{1}{U_o}\underset{S_\perp}{\iint}\underline{n}\,\widetilde{p_w}\,dS \;-\; \frac{1}{U_o}\underset{S_{||}}{\iint}\mu\,\underline{n}\cdot\nabla\,\underline{v}\,dS. \qquad (4.4)
\end{aligned}
$$

The underlined integral is zero since it is assumed that $\overline{p_w}$ is equal for walls E and F. The pressure deviations are caused by shear stress at the transverse surfaces and the pressure deviation integral thus provides the streamwise effect of the transverse integral deleted from equation (4.2). Together the last two integrals thus equal the total pressure drop caused by all shear stresses.

Since the viscosity does not play a significant role in the case of very fast flow, the terms containing it is negligible and equation (4.4) simplifies to

$$-\nabla\langle p\rangle = \frac{d-d_s}{d}\cdot\frac{1}{U_o}\iint_{S_{BB}}\underline{n}\,\overline{p_w}\,dS + \frac{1}{U_o}\iint_{S_\perp}\underline{n}\,\widetilde{p_w}\,dS. \tag{4.5}$$

The first term is treated in the same way it was done for the Darcy regime, while the second is approximated with a drag coefficient term,

$$-\nabla\langle p\rangle = \left(\frac{1}{\psi}-1\right)\nabla\langle p\rangle + \frac{c_d S_{face}\rho w^2}{2U_o}. \tag{4.6}$$

Taking into account that $S_{face}=\frac{1}{4}S_\perp$, equation (4.6) is expressible as

$$-\nabla\langle p\rangle_f = \frac{c_d\rho q^2\psi^3}{8\epsilon^3}\frac{S_\perp}{U_o}. \tag{4.7}$$

The resulting passability for Crosnier et al. (2006) then is,

$$\eta_{Crosnier} = \frac{\epsilon^2(3-\psi)\,d}{c_d\psi^2(\psi-1)}. \tag{4.8}$$

The main difference between the present model and that of Crosnier et al. (2006) is the fact that Crosnier et al. (2006) split the pressure term into a wall average pressure, $\overline{p_w}$, and a pressure deviation, $\widetilde{p}$. This is done because the shear stresses, which occur in the transverse sections, will not contribute to the streamwise component of equation (4.2) and was thus omitted from equation (4.2). These transverse shear stresses are then manifested through the pressure deviation,$\widetilde{p}$. The mathematical effect that this has on the closure modelling procedure done by Crosnier et al. (2006), is contained in the first term on the right hand side of equation (4.6). This term is absent in the present modelling procedure of the inertial term, as discussed in section 2.5.7. The relationship between the passability of the present model, equation (2.94), and that of Crosnier et al. (2006), equation (4.8), is given by,

$$\eta_{crosnier} = \frac{(3-\psi)}{2\epsilon\psi}\eta_{present}. \tag{4.9}$$

For a porosity of 94% equation (4.9) gives

$$\eta_{crosnier} \approx 0.7\eta_{present}. \tag{4.10}$$

These two models for the passability are depicted in Figure 4.2.

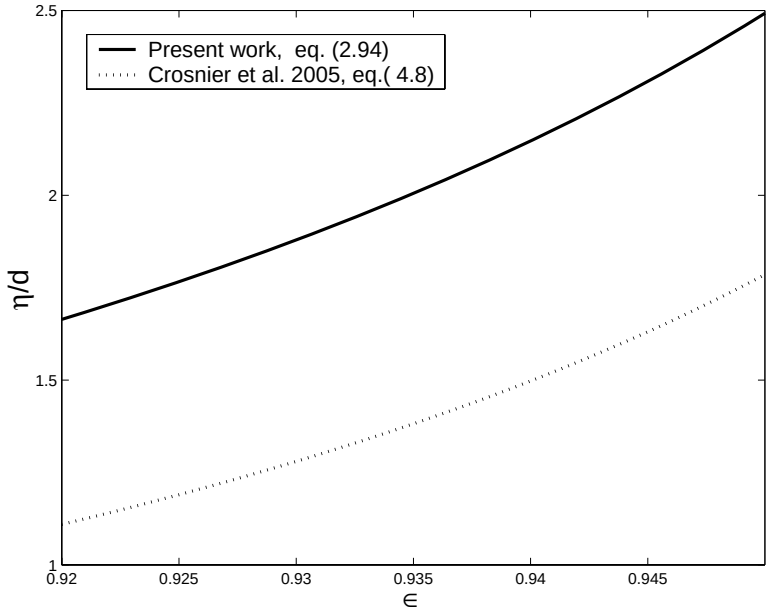

Figure 4.2: Comparison between the present passibility prediction with that of Crosnier et al. (2006) for $c_d = 2$, (equations (2.94) and (4.8)).

Since this work is mainly concerned with the high porosity range, the models are compared to each other for $\epsilon = 0.92$ to $\epsilon = 0.95$ in Figure 4.3.

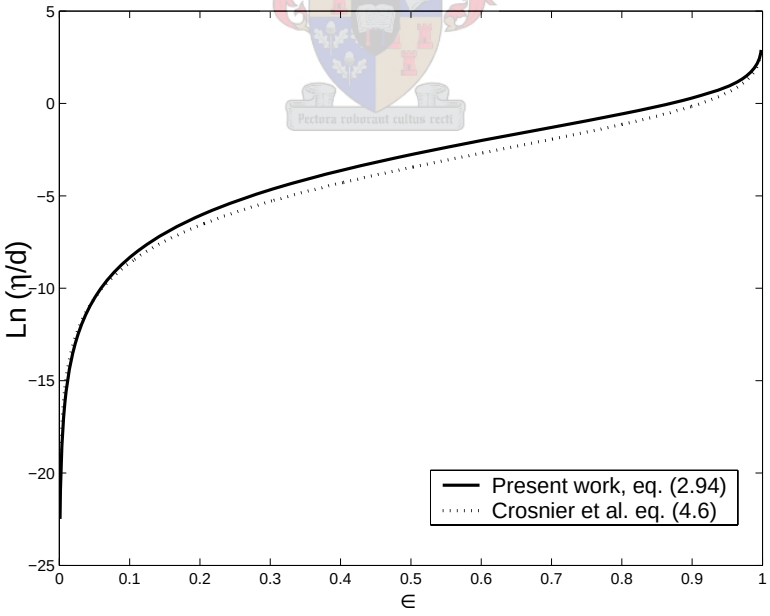

Figure 4.3: Comparison between the present passibility prediction with that of Crosnier et al. (2006) for $c_d = 2$ and $\epsilon > 0.92$, (equations (2.94) and (4.8)).

For the high porosity region, into which metallic foams normally fall, it is clear from Figure 4.3 that the passability predictions of the Crosnier et al. (2006) model is much lower than that of the present model. According to the Crosnier et al. (2006) model the fluid thus moves less easily through the porous medium.

4.1 Comparison with experimental data

4.1.1 Determination of the RRUC dimension and form drag coefficient

The permeability and the passability both depend on the d-dimension of the RUC. Finding a method that is independent of empirical formulaes to predict d is therefore imperative for the validation of the RUC-model.

Linear pressure drop experiments were reported by Crosnier et al. (2006). Letting $M = \frac{c_d}{2d}\frac{\psi(\psi-1)}{\epsilon^3}$ and $N = \frac{36\psi^2(\psi-1)\mu}{\epsilon^2 d^2}$ and rewriting equation (2.101) result in the following expression for the pressure drop

$$\frac{1}{q}\frac{dp}{dx} = M\rho q + N. \tag{4.11}$$

The gradient and the intersection point with the vertical axes can then be read off the empirical straight lines and the experimental values for M_{exp} and N_{exp} determined. These values are then equated to the theoretical expressions for M and N:

$$M_{exp} = \frac{c_d}{2d}\frac{\psi(\psi-1)}{\epsilon^3} \tag{4.12}$$

and

$$N_{exp} = \frac{36\psi^2(\psi-1)\mu}{\epsilon^2 d^2}. \tag{4.13}$$

Equation (4.13) is rewritten and an expression for d obtained as follows:

$$d = \sqrt{\frac{36\psi^2(\psi-1)}{\epsilon^2}\left(\frac{\mu}{N}\right)_{exp}}, \tag{4.14}$$

which can also be written as

$$d = \sqrt{\left(\frac{Nd^2}{\mu}\right)\left(\frac{\mu}{N}\right)_{exp}}. \tag{4.15}$$

An expression for the drag-coefficient, c_d, is obtained in a similar manner, namely

$$c_d = M_{exp}\left(\frac{c_d}{M}\right)_{an}. \tag{4.16}$$

Crosnier et al. (2006) studied three different metal foams: one stainless steel (PORVAIR)– and two aluminium foams (ERG) mainly differing by the number of pores per inch. Examples of these foams are depicted in Figure 4.5. Here only results pertaining to the ERG foams will be discussed. The properties and characteristics of aluminium (ERG) foams are summarised in Table 4.1.

Pressure drop experiments were done by Crosnier et al. (2006) on these foams, and the values for M_{exp} and N_{exp} determined. Image analysis using pictures with deep focus obtained from a microscope allowed Crosnier et al. (2006) to determine the strut diameter distribution for all the foams. Arithmetic means for dm and root mean squares (RMS) of the strand diameters as determined by Crosnier et al. (2006) are given in Table 4.2.

For each foam, Crosnier et al. (2006) determined the ratio, $\frac{dm}{d}$, as can be seen in Table 4.1. The average ratio of the d-value for which a good fit was obtained with respect to the mean strand diameter is 16.5%, (Crosnier et al. (2006)).

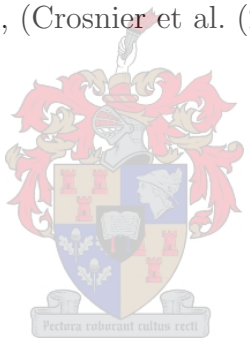

Table 4.1: Properties and characteristics of aluminium foams (ERG).

Doubly staggered foam model									
PPI	Sheet N	Thickness (mm)	ϵ (%)	k 10^7 (m^2)	η 10^3 (m)	Ψ (eq.2.41)	d(mm) (eq.4.15)	c_d (eq.4.16)	dm/d (%)
20	1	20	94.08	1.33	3.68	1.2959	1.6396	1.9349	16.7292
	2		94.12	1.09	3.66	1.2949	1.4799	1.7659	18.5356
	3		93.75	1.29	3.96	1.3045	1.6549	1.7334	16.5754
	1+2	40	94.10	1.23	3.69	1.2954	1.5744	1.8582	17.4224
	1+3		93.91	1.32	3.78	1.3004	1.6544	1.8559	16.5799
	2+3		93.93	1.30	3.72	1.2999	1.6394	1.8739	16.7318
	1+2+3	60	93.98	1.32	3.85	1.2986	1.6458	1.8305	16.6666
10	1	20	94.78	1.83	4.34	1.2769	1.8196	2.0192	17.2232
	2		94.71	1.86	4.32	1.2789	1.8451	2.0350	16.9853
	3		94.76	1.87	4.45	1.2775	1.8425	1.9879	17.0098
	1+2	40	94.74	1.98	4.29	1.2780	1.8990	2.1188	16.5033
	1+3		94.77	2.00	4.46	1.2772	1.9039	2.0527	16.4613
	2+3		94.73	1.93	4.48	1.2783	1.8764	2.0017	16.7019
	1+2+3	60	94.74	2.01	4.59	1.2780	1.9134	1.9952	16.3796

Table 4.2: Properties and characteristics of aluminium foams (ERG) of 20 mm thickness.

Fineness	arithmetic mean of strand diameter dm (μm)
20 ppi	274.3
10 ppi	313.4

Table 4.3: Comparison between analytical and experimental values of d and the corresponding c_d-values.

porosity ϵ %	d_{exp} eq. (4.15)	d_{an} $d_{an} = \frac{100}{16.6} d_m$	$c_d(exp)$ eq. (4.16) $\frac{c_d}{M} = \frac{2d\epsilon^3}{(\psi-1)\psi}$	$c_d(exp_{cros})$ eq. (4.16) $d = d_{exp}$ $\frac{c_d}{M} = \frac{d\epsilon^2(3-\psi)}{(\psi-1)\psi^2}$	$c_d(an_{cros})$ eq. (4.16) $d = d_{an}$ $\frac{c_d}{M} = \frac{d\epsilon^2(3-\psi)}{(\psi-1)\psi^2}$	$c_d(an)$ eq. (4.16) $d = d_{an}$ $\frac{c_d}{M} = \frac{2d\epsilon^3}{(\psi-1)\psi}$	$c_d(fit_{cros})$ eq. (4.17)	$c_d(fit)$ eq. (4.18)
94.08	1.6396	1.6624	1.9349	1.35	1.3710	1.9618	1.2844	1.9091
94.12	1.4799	1.6624	1.7659	1.23	1.3877	1.9838	1.2911	1.9167
93.75	1.6549	1.6624	1.7334	1.20	1.2070	1.7413	1.2336	1.8516
94.10	1.5744	1.6624	1.8582	1.30	1.3719	1.9620	1.2877	1.9129
93.91	1.6544	1.6624	1.8559	1.29	1.2977	1.8649	1.2573	1.8784
93.93	1.6394	1.6624	1.8739	1.31	1.3230	1.9002	1.2604	1.8819
93.98	1.6458	1.6624	1.8305	1.28	1.2889	1.8490	1.2683	1.8908
94.78	1.8196	1.8994	2.0192	1.44	1.5004	2.1077	1.4157	2.0597
94.71	1.8451	1.8994	2.0350	1.45	1.4884	2.0948	1.4011	2.0429
94.76	1.8425	1.8994	1.9879	1.41	1.4580	2.0493	1.4115	2.0549
94.74	1.8990	1.8994	2.1188	1.51	1.5069	2.1192	1.4073	2.0501
94.77	1.9039	1.8994	2.0527	1.46	1.4574	2.0478	1.4136	2.0573
94.73	1.8764	1.8994	2.0017	1.42	1.4404	2.0262	1.4052	2.0477
94.74	1.9134	1.8994	1.9952	1.42	1.4084	1.9807	1.4073	2.0501

An analytical expression for the form drag, c_d, is obtained as follows. The experimental values for d, as given by equation (4.15), are implemented in equation (4.16). These values for the form drag are then plotted and a quadratic fit is done on the data and the corresponding equation recorded. For work done by Crosnier et al. (2006) and the present procedure, these equations are respectively given by,

$$c_d = 325.4\epsilon^2 - 595.8\epsilon + 273.8 \tag{4.17}$$

and

$$c_d = 394\epsilon^2 - 722.6\epsilon + 333. \tag{4.18}$$

The modelling procedure of the inertial terms, used by Crosnier et al. (2006) differs from that used in present work. Two sets of c_d values are therefore plotted in Figure 4.4.

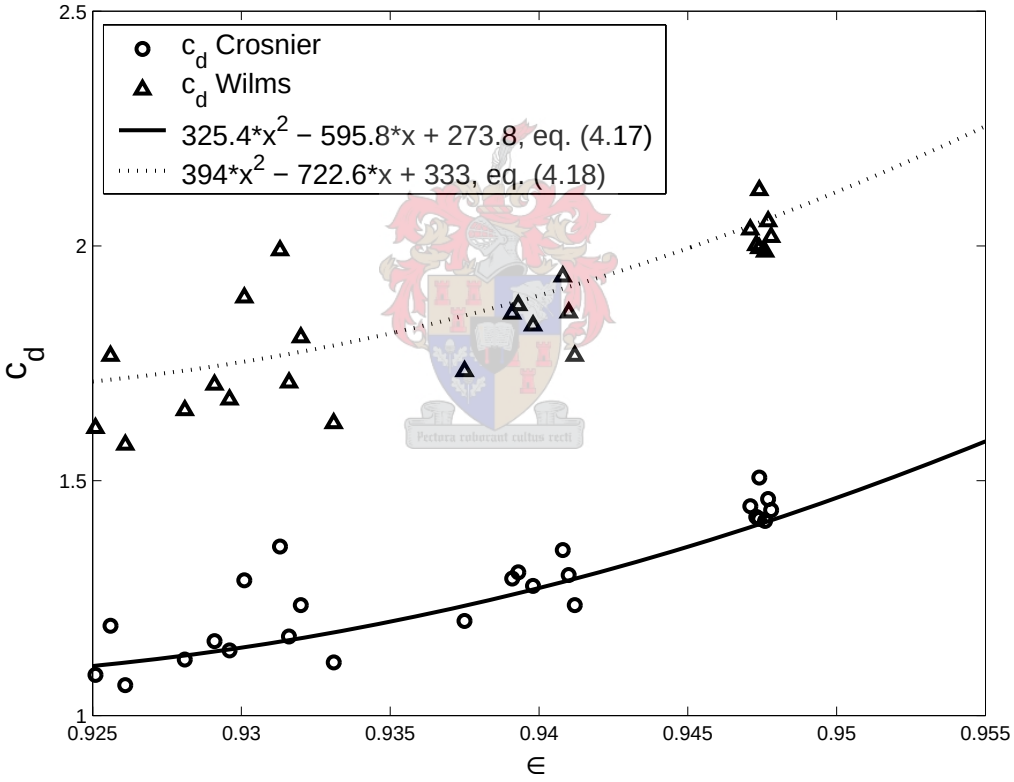

Figure 4.4: Comparison between the drag coefficients.

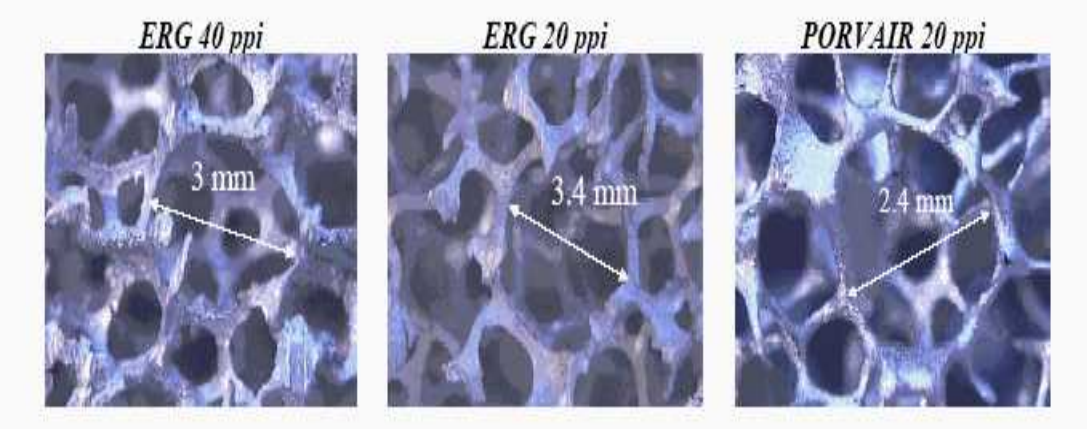

Figure 4.5: Images of foams used by Crosnier et al. (2006).

In the following figures, the present model is evaluated against data supplied by Crosnier et al. (2006) as can be seen in Table 4.1 for $c_d = 2$. These analytical results compare well with the experimental data, as can be seen from Figures 4.6, 4.7, 4.8, 4.9, 4.10 and 4.11. In Figure 4.6 the corresponding pairs of the two sets of data show a high degree of similarity.

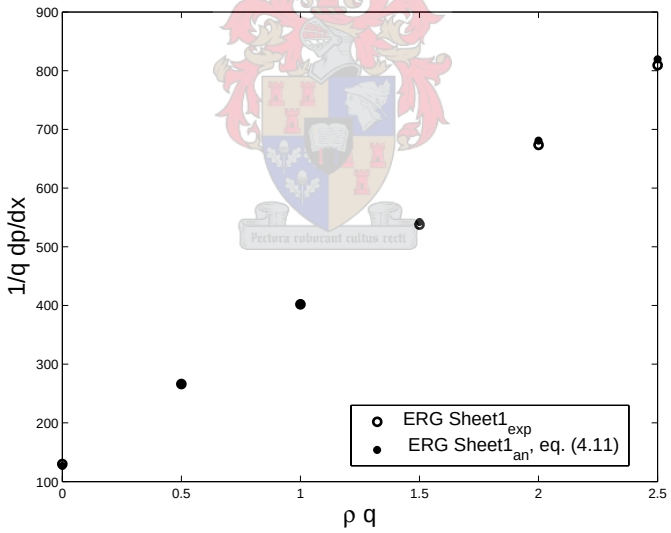

Figure 4.6: Comparison between experimental data (Table 4.1) and analytical model (eq. (4.11)) for sheet 1 of a 20mm thick ERG 20 PPI foam.

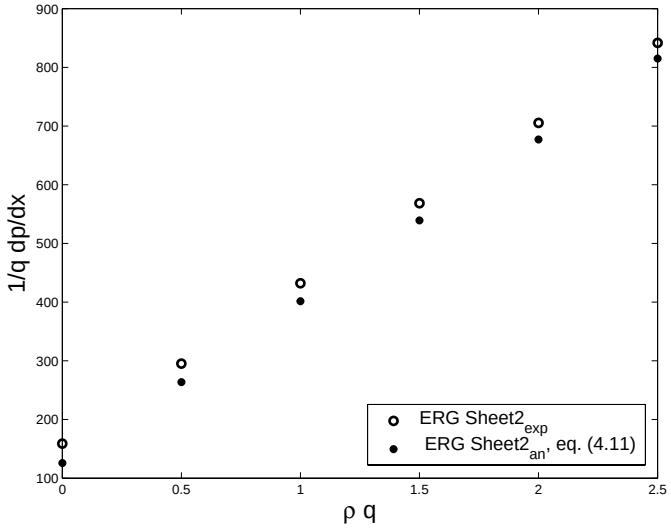

Figure 4.7: Comparison between experimental data (Table 4.1) and analytical model (eq. (4.11)) for sheet 2 of a 20mm thick ERG 20 PPI foam.

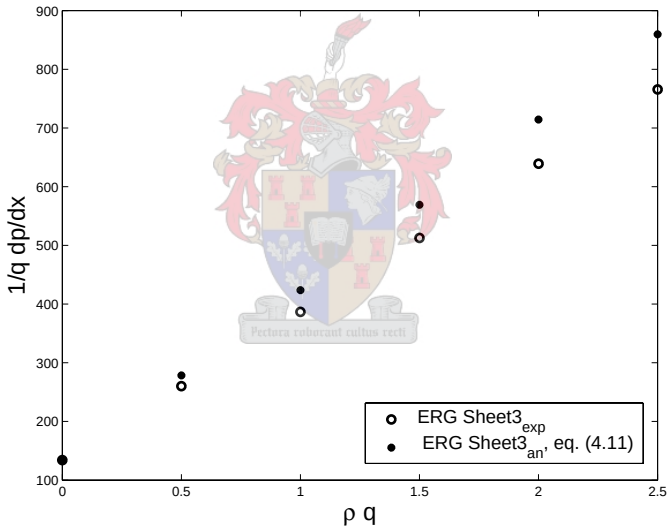

Figure 4.8: Comparison between experimental data (Table 4.1) and analytical model (eq. (4.11)) for sheet 3 of a 20mm thick ERG 20 PPI foam.

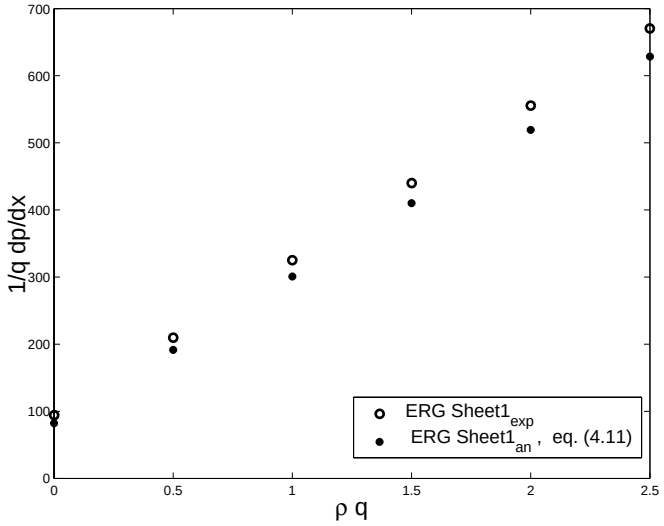

Figure 4.9: Comparison between experimental data (Table 4.1) and analytical model (eq. (4.11)) for sheet 1 of a 20mm thick ERG 10 PPI foam.

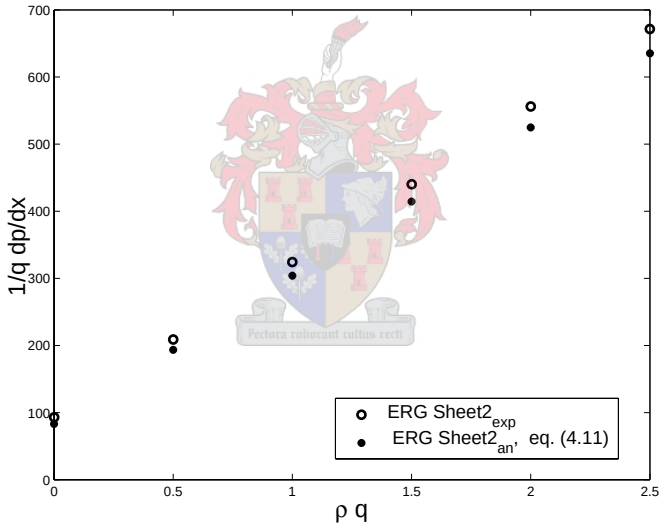

Figure 4.10: Comparison between experimental data (Table 4.1) and analytical model (eq. (4.11)) for sheet 2 of a 20mm thick ERG 10 PPI foam.

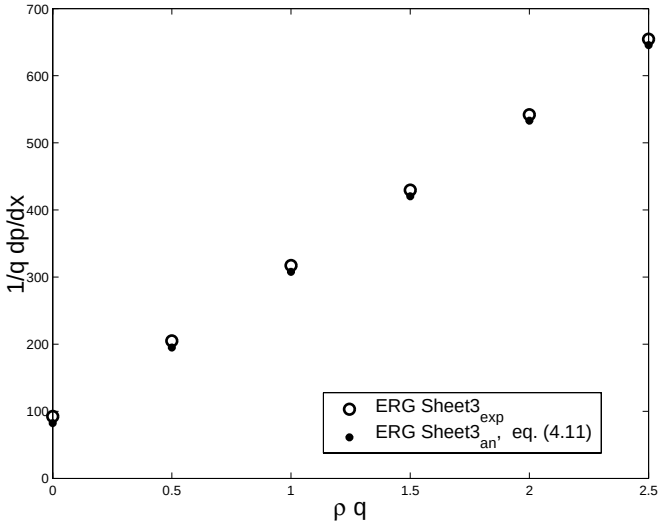

Figure 4.11: Comparison between experimental data (Table 4.1) and analytical model (eq. (4.11)) for sheet 3 of a 20mm thick ERG 10 PPI foam.

From Table 4.3 it is notable that the drag coefficient predicted by the present model, equation (4.18), is higher than that predicted by Crosnier et al. (2006), (equation (4.18)). The model of Crosnier et al. (2006) is reviewed in Addendum C. For a drag coefficient value, $c_d = 1.4$, the pressure drop results are identical to that obtained by the present model with a c_d value of 2. A somewhat higher c_d value for the present model thus results in an almost identical predictive result. Physically this means that more drag is to be added to the present model by increasing the c_d value to better predict the numerical values. This is to be expected since the drag in the transverse channels were simply dropped during the modelling procedure. These drag contributions were taken into account by means of the pressure deviation term in the Crosnier et al. (2006) model. It is therefore concluded that the modelling adaptation for the inertial term, as introduced by Crosnier et al. (2006) is physically more correct.

4.2 Overview of experimental data and model given by Bhattacharya et al.

A short review of the work done by Bhattacharya et al. (2000) is given in this section. Their work was based on the following model, developed by Du Plessis et al. (1994):

$$\frac{K}{d^2} = \frac{\epsilon^2}{36\chi(\chi-1)}. \tag{4.19}$$

The method introduced by Du Plessis et al. (1994) to determine d, namely

$$d = \sqrt{(\frac{\chi}{3\epsilon})}d_p \tag{4.20}$$

was followed. *The only difference between work done by Bhattacharya et al. (2000) and that of Du Plessis et al. (1994) for permeability prediction, is contained in the expression used for tortuosity.* The original expression for the tortuosity of the RUC-model was given by Du Plessis et al. (1994) as

$$\chi = 2 + 2cos\left(\frac{4\pi + arccos(2\epsilon - 1)}{3}\right). \tag{4.21}$$

Bhattacharya et al. (2000) argued that the Du Plessis et al. (1994) model over-predicted the permeability and suggested that this could be rectified by the derivation of a new expression for the tortuosity, χ. It was claimed that the following expression was obtained from Du Plessis (1992),

$$\chi = \frac{\epsilon d_p^2}{A_p} \tag{4.22}$$

where, $A_p = \frac{\pi}{4}(d_p^2 - d_f^2)$, is the cross sectional area of the pore and d_p is the pore diameter. This expression is not only a typing error but was incorrectly cited from Du Plessis (1992) since it is applied in the subsequent theory. The original expression, as was given by Du Plessis (1992), is

$$\chi = \frac{\epsilon d^2}{A_p}. \tag{4.23}$$

Bhattacharya et al. (2000) then derived an expression for χ by applying the relation,

$$\frac{d_f}{d_p} = 1.18\sqrt{\frac{1-\epsilon}{3\pi}}\frac{1}{G} \tag{4.24}$$

to equation (4.22), resulting in,

$$\frac{1}{\chi} = \frac{\pi}{4\epsilon}\left\{1 - \left(1.18\sqrt{\frac{(1-\epsilon)}{3\pi}}\frac{1}{G}\right)^2\right\}. \tag{4.25}$$

Here G is the following geometric function particular to the foam:

$$G = 1 - \exp\left(-\frac{(1-\epsilon)}{0.04}\right). \tag{4.26}$$

Equations (4.22) and (4.21) are depicted in Figure 4.12.

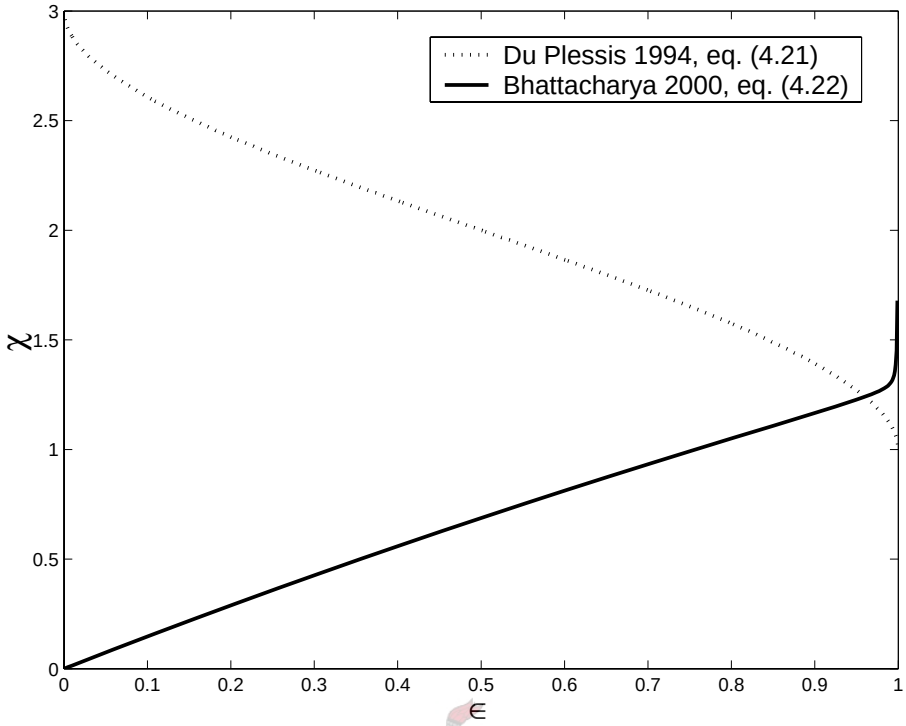

Figure 4.12: Comparison between the tortuosities given by equations (4.22) and (4.21).

From Figure 4.12 the expression for χ, as given by equation (4.22), *increases* as the porosity increases. Physically, this does not make sense. The model resulting from substitution of equation (4.22) into equation (4.19) is given by:

$$K = \frac{\pi\left(1-\frac{0.147738\,(1-\epsilon)}{\left(1-1.38879*10^{-11}\,e^{25\,\epsilon}\right)^2}\right)\epsilon}{144\left(-1+\frac{4\,\epsilon}{\pi+\frac{-2.40639*10^{21}+2.40639*10^{21}\,\epsilon}{\left(7.20049*10^{10}-1.\,e^{25\,\epsilon}\right)^2}}\right)}. \tag{4.27}$$

Equation (4.27) is depicted in Figure 4.13 which again does not make sense from a physical point of view since permeability decreases with an increase in porosity. Furthermore, it can be inferred from equations (4.21) and (4.20) that d and χ are mutually dependent on each other. Equation (4.21) can therefore not be used to determine the determine d since, according to equation (4.20), d is needed to obtain χ. Even though the model derived by Bhattacharya et al. (2000) proved incorrect, their work still provided valuable experimental data, given in Table 4.4, for the verification of the model developed in section 2.5.6 and chapter 3. Equation (4.20) is applied in order to obtain values for d and the correlation between the models and experimental data are presented in Figure 4.14.

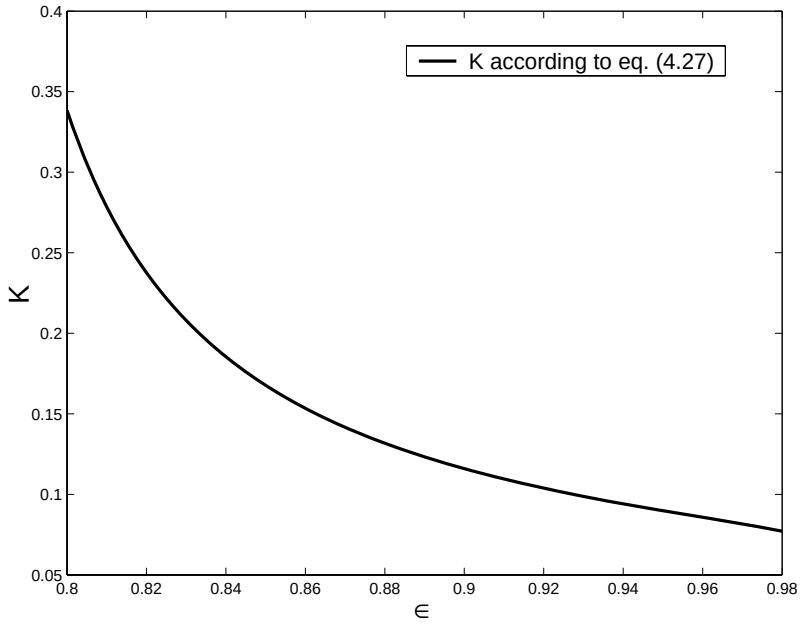

Figure 4.13: Permeability predictions according to Bhattacharya et al. (2000) and equation (4.21).

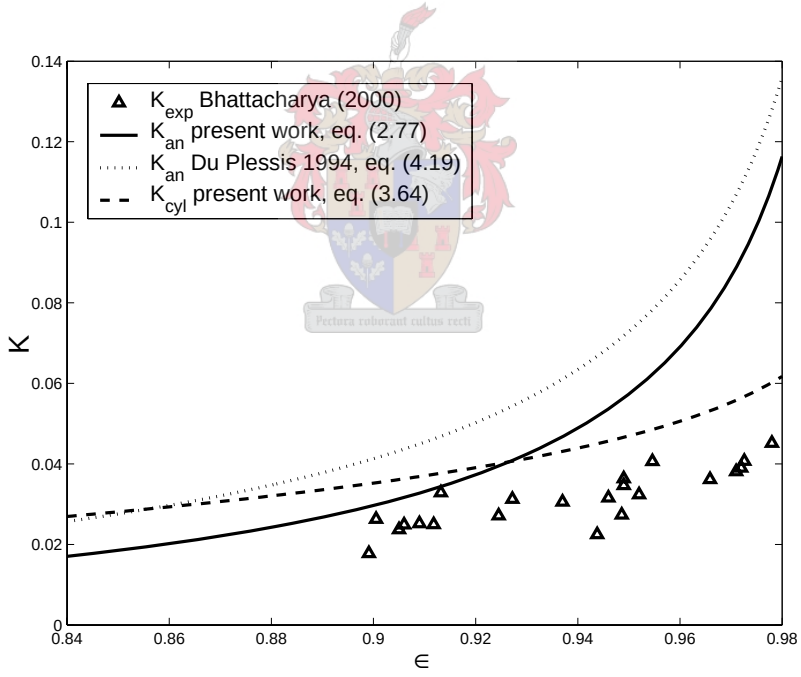

Figure 4.14: Permeability (K) as a function of porosity: experiments vs model (equations (2.77), (4.19) and (3.64)).

K is found to increase with ϵ. This seems physically plausible since the fiber diameter decreases with increase in porosity. As a result the open cross-sectional area available for

fluid flow increases, which reduces flow resistance. Hence K is expected to increase with porosity. In the limiting case when ϵ approaches 1, the value of K should approach infinity (since the porous medium ceases to exist and hence the effect of viscous drag tends to zero.)

The present model still seems to over-predict the permeability, but shows significant improvement on the Du Plessis et al. (1994) model. The cylindrical RUC model seems to predict the experimental trend best. This could be attributed to viscous shear stresses that are replaced by a deformation of the flow field. In other words, the fact that, at high porosities, the flow is predominantly *past* the cylindrical structure instead of *through* it. As a result, the retardation effect on the fluid is greater at high porosities and the permeability growth slower for the cylindrical model. This fact suggests the development of a future model that follows the RUC concept, but incorporates a "flow by" configuration with respect to the interstitial streamlines.

Table 4.4: Characteristics of metal foam samples used for pressure drop experiments, Bhattacharya et al. (2000).

Sample	Porosity	PPI	$d_f * 10^3$ (m)	$d_p * 10^3$ (m)	$K * 10^7$
1	0.9726	5	0.5000	4.0200	2.7000
2	0.9118	5	0.5500	3.8000	1.8000
3	0.9486	10	0.4000	3.1300	1.2000
4	0.9438	10	0.4500	3.2800	1.1000
5	0.8991	10	0.4300	3.2000	0.9400
6	0.9546	20	0.3000	2.7000	1.3000
7	0.9245	20	0.3500	2.9000	1.1000
8	0.9005	20	0.3500	2.5800	0.9000
9	0.9659	40	0.2000	1.9000	0.5500
10	0.9272	40	0.2500	2.0200	0.6100
11	0.9132	40	0.2000	1.8000	0.5300
12	0.9710	5	0.5100	4.0000	2.5200
13	0.9460	5	0.4700	3.9000	2.1700
14	0.9050	5	0.4900	3.8000	1.7400
15	0.9490	10	0.3700	3.1000	1.4900
16	0.9090	10	0.3800	2.9600	1.1100
17	0.9780	20	0.3800	2.8000	1.4200
18	0.9490	20	0.3200	2.7000	1.1850
19	0.9060	20	0.3400	2.6000	0.8540
20	0.9720	40	0.2300	1.8000	0.5200
21	0.9520	40	0.2400	1.9800	0.5620
22	0.9370	40	0.2400	2.0000	0.5680

Chapter 5

Conclusions

The model of Du Plessis et al. (1994) is extended in this work by making provision for the RUC boundaries to cut through both solid and fluid sections. In doing so it better represents the REV and thus the material to be modelled. The inclusion of stagnant regions makes provision for the scenario where void sections in the foam exist during fluid flow. The pressure in each transverse section is also split into a wall pressure average, $\overline{p}$, and a pressure deviation, $\widetilde{p}$. This pressure deviation then takes into account the pressure loss due to shear stresses in the transverse channel sections.

This work includes a modelling procedure for the Forchheimer regime and use of an asymptotic matching technique by Churchill & Usagi (1972) enables the construction of a momentum equation that can predict flow for the entire range of laminar flows inclusive of inertial effects. Following work done by Smit et al. (2005), the model is extended to include the discharge of a particular non-Newtonian flow through metallic foams.

In this work the assumption is made that the average wall pressure on opposing walls in the transverse sections of an RUC cutting through solid sections is equal and cancels. This is merely an assumption, not a certainty, and should in future be investigated further by numerical simulation. The use of cylinders showed a substantial difference in permeability prediction. Instead of viscous shearing stress the cylinders causes a deformation of the flow field which at high porosities increases retardation of fluid movement. Mathematically this model is however far more complex than the original RUC-model and does not make provision for generalisation to non-Newtonian flow since the assumption of Newton flow was assumed during the modelling procedure.

Further modifications, which are yet to be published, have been made to the current model by Crosnier et al. (2006). These modifications concern the modelling of the inertial effect. The pressure term is divided into an average pressure and a pressure deviation term. This is in effect the only difference between the work of Crosnier et al. (2006) and the present modelling procedure.

The development of the RUC model since it was first introduced in 1988 is briefly sum-

marised in Table 5.1.

At first glance, the RUC model seems to over simplify the material to be modelled. Yet, geometrical more complicated models, such as were introduced by Fourie & Du Plessis (2001), have not shown significant improvement or, in the case of the cylindrical model, cannot be extended to cover non-Newtonian flow. In the absence of fudge factors the current RUC-model provides a simple yet accurate modelling procedure for complex structures.

Possible future work could include a numerical investigation into the flow in transverse sections of the RUC-model in order to verify assumptions made regarding the average wall pressure.

Table 5.1: Development of the RUC model

Authors	Development
Du Plessis & Masliyah (1988)	RUC-model is introduced.
Du Plessis et al. (1994)	RUC is extended to the Forchheimer regime. The RUC side length, d, is experimentally determined.
Bhattacharya et al. (2000)	Shape factor, G, is introduced. A new expression for tortuosity is derived. χ is defined incorrectly. As a result, the model is faulty.
Fourie & Du Plessis (2001)	A tetrakaidecahedral shape is introduced to construct an analytical expression for d. The model proves redundant since a similar result is achieve by Du Plessis et al. (1994).
Lloyd et al. (2004)	A pressure modelling correction is made for two dimensional flow. Provision is made for RUC boundaries to cut through both solid and fluid sections and both scenarios are weighed according to relative frequency of occurrence.
Smit et al. (2005)	The RUC model is extended to non-Newtonian flow.
Present work 2005	Void sections are introduced. Modifications by Lloyd et al. (2004) are extended to three dimensions. Following Crosnier et al. (2006), an analytical expression for d is constructed.
Crosnier et al. (2006)	A correction is made to the modelling procedure for inertial flow: The pressure is split into an average and a deviation term.

Bibliography

Bear, J. & Bachmat, Y. (1991). *Introduction to modelling of transport phenomena in porous media*. Kluwer Academic Publishers, Dordrecht.

Bhattacharya, A., Calmidi, V. V., & Mahajan, R. L. (2000). Thermophysical properties of high porosity meal foams. *International Journal of Heat an Mass Transfer*, *45*, 1017–1031.

Carman, P. C. (1937). Fluid flow through granular beds. *Transactions of the Institution of Chemical Engineers*, *15*, 150–166.

Carman, P. (1956). *Flow Of Gases Through Porous Media*. Butterworths Scientific Publications.

Churchill, S. W. & Usagi, R. (1972). A general expression for the correlation of rates of transfer and other phenomena. *AIChe Journal*, *18*(6), 1121–1128.

Crosnier, S., Du Plessis, J. P., Riva, R., & Legrand, J. (2006). Modelling of gas flow through isotropic metallic foams. *Journal of Porous Media*. To be published.

Diedericks, G. P. J. & Du Plessis, J. P. (1995). On tortuosity and areosity tensors for porous media. *Transport in Porous Media*, *20*, 265–279.

Du Plessis, J. P. & Masliyah, J. H. (1988). Mathematical modelling of flow through consolidated isotropic porous media. *Transport in Porous Media*, *3*, 145–161.

Du Plessis, J. P., Montillet, A., Comiti, J., & Legrand, J. (1994). Pressure drop prediction for flow through high porosity metallic foams. *Chemical Engineering Science*, *49*(21), 3545–3553.

Fourie, J. G. & Du Plessis, J. P. (2001). Pressure drop modelling in cellular metallic foams. *Chemical Engineering Science*, *57*, 2781–2789.

Happel, J. & Brenner, H. (1983). *Low Reynolds number hydrodynamics*. Martinus Nijhoff Publishers.

Happel, J. (1959). Viscous flow relative to arrays of cylinders. *A.I.Ch.E.*, *2*, 174–177.

Hughes & Gaylord (1964). *Engineering Science*. Schaum Publishing Co.

Lloyd, C. A., Du Plessis, J. P., & Halvorsen, B. M. (2004). On closure modelling of volume averaged equations for flow through two-dimensional arrays of squares. *Proceedings of the Fifth International Conference on Advances in Fluid Mechanics, AFM 2004, Lisbon, Portugal*, 85–93.

Smit, G. J. F., Du Plessis, J. P., & Wilms, J. M. (2005). On the modelling of non-Newtonian purely viscous flow through high porosity synthetic foams. *Chemical Engineering Science*, *60*, 2815–2819.

Spiegel, R. M. (1968). *Mathematical Handbook of Formulas and Tables*. McGraw-Hill.

Whitaker, S. (1996). *Fluid Transport in Porous Media, ed. Prieur du Plessis*, volume 13 of *International series on Advances in Fluid Mechanics*, chapter 1: Volume averaging of Transport Equations, (pp. 1–60). Computational Mechanics Publications.

Wilms, J. M., Du Plessis, J. P., & Smit, G. J. F. (March 2005). Modelling of flow in foamlike porous media. *Proceedings of the International Conference on Environmental Fluid Mechanics, Guwahati, India*, 270–276.

Appendix A

A.1 Tortuosity

The tortuosity of a porous medium is loosely defined as the ratio of the average streamline length in a domain to the actual displacement in the domain.

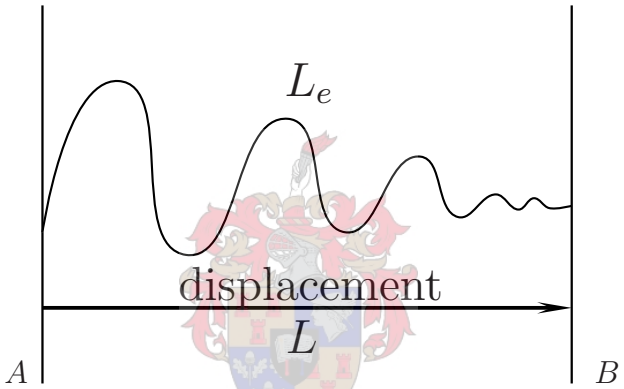

Figure A.1: Tortuosity of a streamline.

In Figure A.1 is shown a simple schematic illustration of the tortuosity of a streamline being defined as the ratio of the length, L_e, of a single streamline between two planes A and B and the displacement, L, between the two planes, namely

$$\chi = \frac{L_e}{L}. \tag{A.1}$$

Carman (1937) realised that the path taken by the fluid is not a straight line but tortuous. The velocity inside the fluid volume therefore has to be greater than predicted by equation (2.9) which was equated under the assumption that the path is straight. The drift velocity, $\underline{u}$, therefore should be multiplied by this fractional increase in path length which, according to equation (A.1), is merely the tortuosity, χ.

The argument can also be based on the existing model given by equation (2.10): Equation (A.1) is a measure of the tortuosity of every streamline. If all the streamlines are taken together the tortuosity can be rewritten as

$$\chi \;=\; \frac{\mathcal{U}_f}{\mathcal{U}_L}. \tag{A.2}$$

From equation (2.10) it follows that

$$\underline{w} \;\equiv\; \frac{1}{\mathcal{U}_{\mathcal{L}}} \iiint\limits_{\mathcal{U}_f} \underline{v}\, d\mathcal{U} \;=\; \frac{U_o}{\mathcal{U}_{\mathcal{L}}}\, \underline{q} \;=\; \frac{\mathcal{U}_f}{\epsilon \mathcal{U}_{\mathcal{L}}}\, \underline{q}. \tag{A.3}$$

It thus follows that

$$\underline{w} \;=\; \frac{\chi}{\epsilon}\, \underline{q}, \tag{A.4}$$

which is the Carman adaptation, (Carman, 1937), to the Dupuit-Forchheimer relationship. The porosity of the RRUC must be the same as that of the REV it represents, so that, analogous to equation (2.5):

$$\epsilon \;=\; \frac{U_f}{U_o}. \tag{A.5}$$

In Figure A.2 is shown the geometry of an RRUC for a foamlike material introduced by Du Plessis & Masliyah (1988).

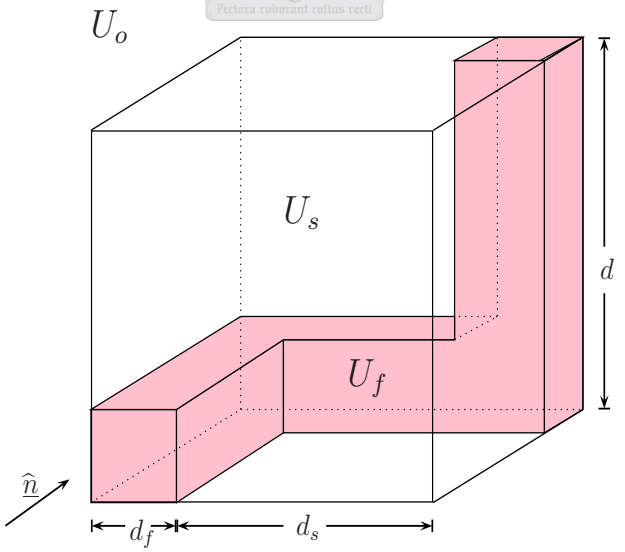

Figure A.2: Geometry of RRUC model for an isotropic metallic foam ($\epsilon \approx 0.2$).

The shaded volume represents the void part contained within a cube of side length, d. The configuration in Figure A.2 is drawn for a porosity of about 0.2. From equation (A.5) the porosity of the model in Figure A.2 can be expressed in terms of the RRUC parameters as

$$\epsilon \;=\; \frac{3d_f^2 d - 2d_f^3}{d^3} \;=\; \left(\frac{d_f}{d}\right)^2 \left(3 - 2\frac{d_f}{d}\right). \tag{A.6}$$

The assumption of piece-wise plane Poiseuille flow in each duct section suggests a bundle of straight streamlines in each duct section.

A.1.1 Over-staggered model

In case of the over-staggered model, the fluid is assumed to traverse all three void channels as is shown in Figure A.3.

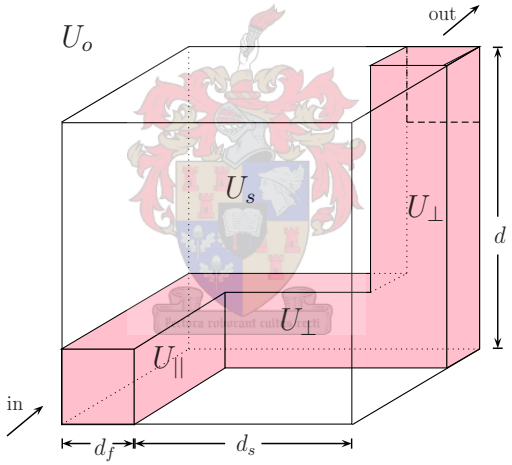

Figure A.3: RRUC for the over-staggered foam model.

The tortuosity of every streamline in the over-staggered RRUC is therefore given by

$$\chi \;=\; \frac{d + 2d_s}{d} \;=\; 1 \;+\; 2\frac{d_s}{d} \;=\; 3 \;-\; 2\frac{d_f}{d}. \tag{A.7}$$

From equation (A.6) it then follows that

$$\chi^3 - 6\chi^2 + 9\chi - 4\epsilon \;=\; 0. \tag{A.8}$$

Solution of equation(A.8) with boundary conditions

$$\epsilon = 1 \text{ if } \chi = 1. \tag{A.9}$$

yields by means of the Cardanic method (Appendix A.2):

$$\chi \;=\; 2 \;+ 2 \;\cos\left[\frac{4\pi + \cos^{-1}(2\epsilon - 1)}{3}\right]. \tag{A.10}$$

Equation A.10 is graphically presented in Figure A.4.

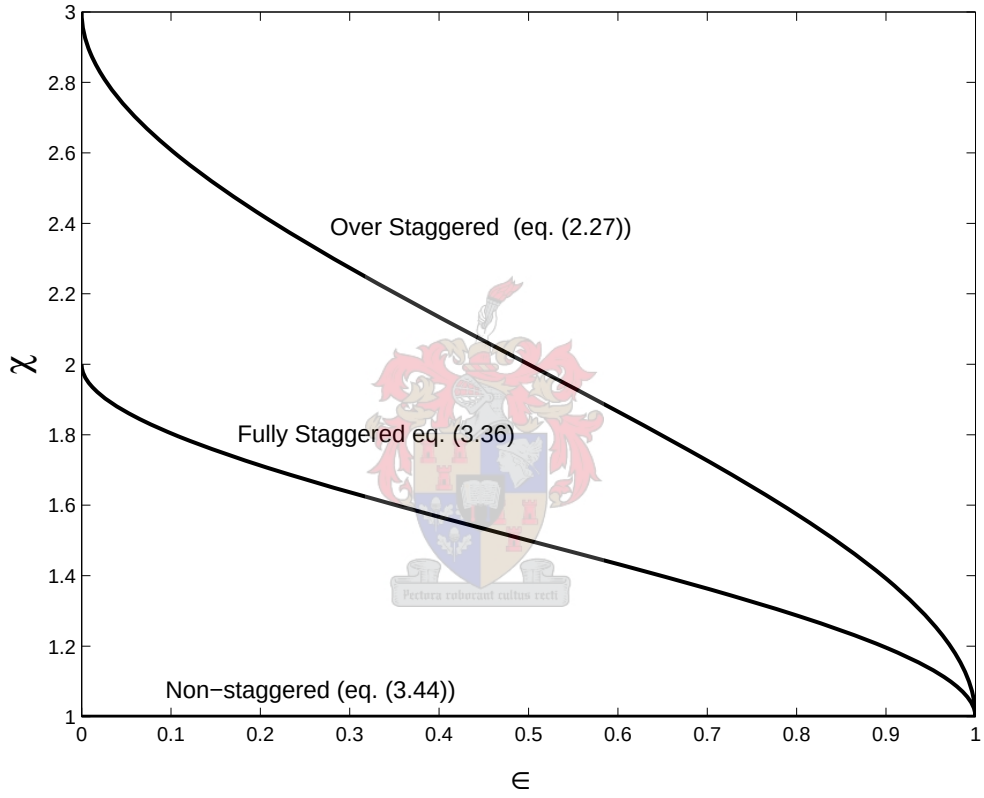

Figure A.4: The geometric tortuosity of the metallic foam models.

A.1.2 Fully staggered model

In case of the fully staggered model, one of the three void arms of the RRUC contains stagnant fluid and is thus a dead zone as is shown in Figure A.5. This results in a

tortuosity of

$$\chi \;=\; \frac{2d - d_f}{d} \;=\; 2 - \frac{d_f}{d}. \tag{A.11}$$

Substitution of

$$\frac{d_f}{d} \;=\; 2 - \chi \tag{A.12}$$

into equation (A.6) yields

$$\epsilon \;=\; 3\,(2-\chi)^2 - 2\,(2-\chi)^3\,. \tag{A.13}$$

This results in the following cubic polynomial in χ to be solved for χ

$$0 \;=\; \chi^3 - \frac{9}{2}\chi^2 + 6\chi - 2 - \frac{1}{2}\epsilon \tag{A.14}$$

also subject to boundary condition (A.9) so that the solution for χ in the fully staggered case according to, A.2, is:

$$\chi \;=\; \frac{3}{2} + \cos[\frac{1}{3}\arccos(2\epsilon - 1) + \frac{4}{3}\pi]. \tag{A.15}$$

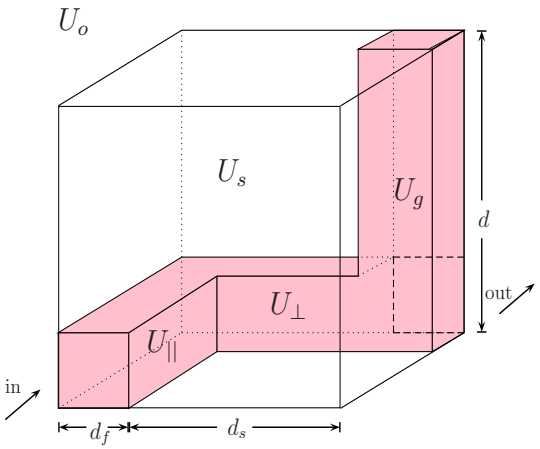

Figure A.5: RRUC for the fully staggered foam model.

Equation (A.15) is presented graphically in Figure A.4.

The expression (A.15) for the tortuosity of a fully staggered configuration can also be obtained using the following line of reasoning:

From equation (A.11) and equation (A.7) respectively it follows that

$$\chi_{\text{fully}} = 2 - \frac{d_f}{d} \tag{A.16}$$

and

$$\chi_{\text{over}} = 3 - 2\frac{d_f}{d}. \tag{A.17}$$

Writing equation (A.16) in terms of equation (A.17) and using equation (A.10) it then follows that:

$$\chi_{\text{fully}} = \chi_{\text{over}} - 1 + \frac{d_f}{d} \tag{A.18}$$

$$= \chi_{\text{over}} + 2 - \chi_{\text{fully}} \tag{A.19}$$

$$= \frac{3}{2} + \cos\left[\frac{\arccos(2\epsilon - 1)}{3} + \frac{4}{3}\pi\right], \tag{A.20}$$

again yielding equation (A.15).

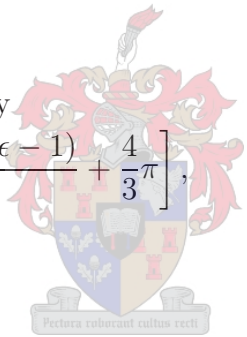

A.1.3 Non-staggered model

In case of the non staggered model, the fluid only passes through one channel as is presented in Figure A.6.

If the fluid is assumed to traverse only one of the three channels leaving the other two stagnant, the geometric tortuosity, in terms of RRUC geometry is determined as:

$$\chi = \frac{d}{d} = 1. \tag{A.21}$$

and graphically presented in Figure A.4.

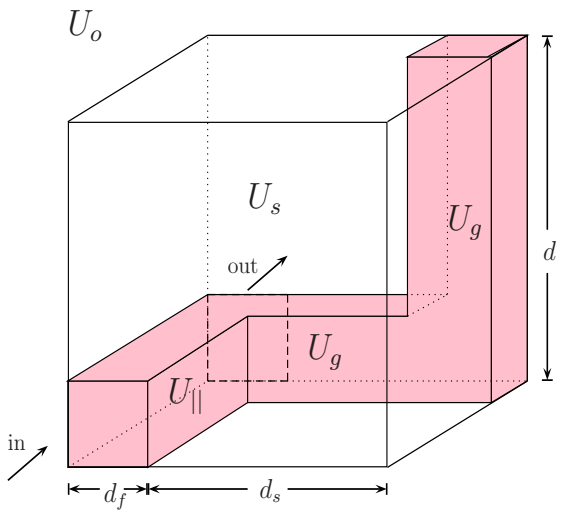

Figure A.6: RRUC for the non-staggered foam model.

A.2 Cardanic method of solving a cubic polynomial

The following *Cardanic Method* may be used to solve cubic polynomials. Suppose the following cubic is to be solved:

$$x^3 + a_1x^2 + a_2x + a_3 = 0. \tag{A.22}$$

Let

$$Q = \frac{3a_2 - a_1^2}{9} \tag{A.23}$$

$$R = \frac{9a_1a_2 - 27a_3 - 2a_1^3}{54} \tag{A.24}$$

$$S = \sqrt[3]{R + \sqrt{Q^3 + R^2}} \tag{A.25}$$

$$T = \sqrt[3]{R - \sqrt{Q^3 + R^2}}. \tag{A.26}$$

Solutions to A.1 are then:

$$x_1 = S + T - \frac{1}{3}a_1 \tag{A.27}$$

$$x_2 = -\frac{1}{2}(S + T) - \frac{1}{3}a_1 + \frac{1}{2}i\sqrt{3}(S - T) \tag{A.28}$$

$$x_3 = -\frac{1}{2}(S + T) - \frac{1}{3}a_1 - \frac{1}{2}i\sqrt{3}(S - T). \tag{A.29}$$

If $a_1,\ a_2,\ a_3$ are real and if $D = Q^3 + R^2$ is the *discriminant*, then

- one root is real and two complex conjugate if D > 0
- all roots are real and at least two are equal if D $= 0$
- all roots are real and unequal if D < 0.

If D < 0, computation is simplified by use of trigonometry and the following three solutions exist, with $\cos\Theta = \frac{R}{\sqrt{-Q^3}}$
Solutions if D $<$ 0:

$$\begin{aligned} x_1 &= 2\sqrt{-Q}\cos\left(\frac{1}{3}\Theta\right) - \frac{1}{3}a_1 \\ x_2 &= 2\sqrt{-Q}\cos\left(\frac{1}{3}\Theta + \frac{2}{3}\pi\right) - \frac{1}{3}a_1 \\ x_3 &= 2\sqrt{-Q}\cos\left(\frac{1}{3}\Theta + \frac{4}{3}\pi\right) - \frac{1}{3}a_1. \end{aligned}$$

Note:
The method described in the Mathematical handbook of Formulas and Tables by Spiegel (1968) contains an error in the trigonometric simplification in that it omits the $-a_1$ factor that should be present if a correct answer is to be arrived at.
The equations ought to be:

$$\begin{aligned} x_1 + x_2 + x_3 &= -a_1 \\ x_1x_2 + x_2x_3 + x_3x_1 &= a_2 \\ x_1x_2x_3 &= a_3 \end{aligned}$$

where $x_1,\ x_2,\ x_3$ are the three roots.

Appendix B

B.1 Derivation of constants for the biharmonic equation

In this section expressions for the four constants in the following equation is determined.

$$\psi = \sin\theta\left[\frac{1}{8}Cr^3 + \frac{1}{2}Dr(\ln r - \frac{1}{2}) + Er + \frac{F}{r}\right]. \tag{B.1}$$

Application of definitions, $v_r = \frac{1}{r}\frac{\partial\psi}{\partial\theta}$, and, $v_\theta = -\frac{\partial\psi}{\partial r}$, results in the following expressions

$$v_r = \cos\theta\left[\frac{1}{8}Cr^2 + \frac{1}{2}D(\ln r - \frac{1}{2}) + E + Fr^{-2}\right] \tag{B.2}$$

and

$$v_\theta = -\sin\theta\left[\frac{3}{8}Cr^2 + \frac{1}{2}D(\frac{1}{2} + \ln r) + E - Fr^{-2}\right]. \tag{B.3}$$

The following boundary values are imposed at $r = a$ for the cylindrical surfaces moving rectilinearly with speed $\underline{u}$:

$$v_r = U\cos\theta \tag{B.4}$$

and

$$v_\theta = -U\sin\theta. \tag{B.5}$$

From equations (B.4) and (B.2) we have

$$U = \frac{1}{8}Ca^2 + \frac{1}{2}D(\ln a - \frac{1}{2}) + E + Fa^{-2}, \tag{B.6}$$

and from equations (B.5) and (B.2):

$$U = \frac{3}{8}Ca^2 + \frac{1}{2}D(\frac{1}{2} + \ln a) + E - Fa^{-2} \tag{B.7}$$

At $r = b$ the following boundary conditions are imposed:

$$v_r = 0 \tag{B.8}$$

and

$$0 = \frac{\partial v_\theta}{\partial r} + \frac{1}{r}\frac{\partial v_r}{\partial \theta} - \frac{v_\theta}{r}. \tag{B.9}$$

From equations (B.8) and (B.2) it ten follows that

$$0 = \cos\theta \left[\frac{1}{8}Cb^2 + \frac{1}{2}D(\ln b - \frac{1}{2}) + E + Fb^{-2}\right]. \tag{B.10}$$

From equations (B.9) and (B.2) it also follows that

$$\begin{aligned} 0 = & -\sin\theta \left[\frac{3}{4}Cb + \frac{1}{2}Db^{-1} + 2Fb^{-3}\right] \\ & -\sin\theta \left[\frac{1}{8}Cb + \frac{1}{2}D(b^{-1}\ln r - \frac{1}{2}b^{-1}) + Eb^{-1} + Fb^{-3}\right] \\ & +\sin\theta \left[\frac{3}{8}Cb + \frac{1}{4}Db^{-1} + \frac{1}{2}Db^{-1}\ln r + Eb^{-1} - Fb^{-3}\right] \end{aligned} \tag{B.11}$$

$$\begin{aligned} 0 = & -\sin\theta \left[\frac{1}{2}Cb + \frac{1}{4}Db^{-1} + \frac{1}{2}D(b^{-1}\ln b - \frac{1}{2}b^{-1})\right. \\ & \left. -\frac{1}{2}Db^{-1}\ln b + 4Fb^{-3}\right] \end{aligned} \tag{B.12}$$

$$0 = \frac{1}{2}Cb + 4Fb^{-3} \tag{B.13}$$

$$0 = Cb + 8Fb^{-3} \tag{B.14}$$

From equation (B.14) we thus have:

$$F = -\frac{Cb^4}{8} \tag{B.15}$$

Substitution of equation (B.15) into equation (B.10) yields:

$$0 = \frac{1}{8}Cb^2 - \frac{Cb^4}{8}b^{-2} + \frac{1}{2}D(\ln b - \frac{1}{2}) + E$$

so that

$$\Rightarrow E = -\frac{1}{2}D(\ln b - \frac{1}{2}). \tag{B.16}$$

Substitution of equations (B.15) and (B.16) into equation (B.7):

$$\begin{aligned} U &= \frac{3}{8}Ca^2 + \frac{1}{2}D(\frac{1}{2} + \ln a) - \frac{1}{2}D(\ln b - \frac{1}{2}) - \left(-\frac{Cb^4}{8}\right)a^{-2} \\ &= \frac{3}{8}Ca^2 + \frac{Cb^4}{8a^2} + \frac{1}{2}D(1 + \ln a - \ln b) \end{aligned} \tag{B.17}$$

From equation (B.17) it now follows that:

$$U = \frac{C}{8}\left[3a^2 + \frac{b^4}{a^2}\right] + \frac{D}{2}\left[1 + \ln a - \ln b\right]$$

So that

$$C = \frac{a^2}{3a^4 + b^4}\left[8U - 4D\left(1 + \ln\frac{a}{b}\right)\right]. \tag{B.18}$$

Substitution of equations (B.15) and (B.16) into (B.6) yields:

$$\begin{aligned} U &= \frac{1}{8}Ca^2 + \frac{1}{2}D(\ln a - \frac{1}{2}) - \frac{1}{2}D(\ln b - \frac{1}{2}) + \left(-\frac{Cb^4}{8}\right)a^{-2} \\ &= \frac{1}{8}Ca^2 - \frac{Cb^4}{8a^2} + \frac{1}{2}D(\ln a - \ln b) \end{aligned} \tag{B.19}$$

From equation (B.19) it then follows that:

$$U = \frac{C}{8}(a^2 - \frac{b^4}{a^2}) + \frac{1}{2}D\ln\frac{a}{b}.$$

It follows that

$$C = \frac{a^2}{a^4 - b^4}\left[8U - 4D\ln\frac{a}{b}\right]. \tag{B.20}$$

Substitution of equation (B.18) into (B.20) yields:

$$\frac{a^2}{3a^4+b^4}\left[8U-4D\left(1+\ln\frac{a}{b}\right)\right] \;=\; \frac{a^2}{a^4-b^4}\left[8U-4D\ln\frac{a}{b}\right],$$

it follows that

$$\begin{aligned}24\,a^4U-12a^4D\ln\frac{a}{b}+8b^4U-4b^4D\ln\frac{a}{b} \;&=\; a^4 8U-a^4 4D(1+\ln\frac{a}{b})-b^4 8U\\ &\quad +4b^4D(1+\ln\frac{a}{b}).\end{aligned}$$

Therefore

$$D \;=\; \frac{4U(a^4+b^4)}{2\ln\frac{a}{b}(a^4+b^4)-(a^4-b^4)} \;=\; \frac{4U(a^4+b^4)}{2(a^4+b^4)\ln a-2(a^4+b^4)\ln b-a^4+b^4} \qquad \text{(B.21)}$$

From equation (B.20) it is then obtained that

$$\begin{aligned}C \;&=\; \frac{a^2}{a^4-b^4}\left[8U-\frac{16U(a^4+b^4)\ln\frac{a}{b}}{2\ln\frac{a}{b}(a^4+b^4)-a^4+b^4}\right]\\ &=\; \frac{8Ua^2}{a^4-b^4}-\frac{a^2}{a^4-b^4}\left[\frac{16U(a^4+b^4)\ln\frac{a}{b}}{2\ln\frac{a}{b}-a^4+b^4}\right]\\ &=\; \frac{16Ua^2\ln\frac{a}{b}(a^4+b^4)+8Ua^2(-a^4+b^4)-a^2 16U(a^4+b^4)\ln\frac{a}{b}}{(a^4-b^4)\left[2\ln\frac{a}{b}(a^4+b^4)-a^4+b^4\right]}\\ &=\; \frac{-8Ua^2}{2\ln a(a^4+b^4)-2\ln b(a^4+b^4)-a^4+b^4}. \qquad \text{(B.22)}\end{aligned}$$

Subsequently from equation (B.15):

$$F \;=\; \frac{Ua^2b^4}{2\ln a(a^4+b^4)-2\ln b(a^4+b^4)-a^4+b^4}. \qquad \text{(B.23)}$$

Lastly from from equation (B.16) it follows that

$$\begin{aligned}E \;&=\; \frac{-\frac{1}{2}(\ln b-\frac{1}{2})4U(a^4+b^4)}{2(a^4+b^4)\ln a-2(a^4+b^4)\ln b-a^4+b^4}\\ &=\; \frac{(2\ln b-1)U(a^4+b^4)}{-2(a^4+b^4)\ln a+2(a^4+b^4)\ln b+a^4-b^4}. \qquad \text{(B.24)}\end{aligned}$$

Appendix C
Experimental verification of model developed by Crosnier et al. (2006)

The correlation between experimental data and the Crosnier et al. (2006) model for a drag coefficient value, $c_d = 2$, is depicted in Figures C.1, C.2, C.3, C.4, C.5 and C.6.

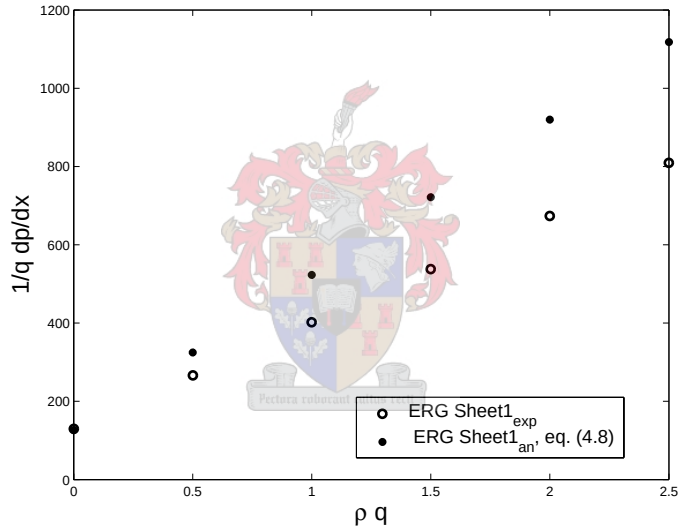

Figure C.1: Comparison between experimental data (Table 4.1) and Crosnier et al. (2006) model with the inertial term given by eq. (4.8) for sheet 1 of a 20mm thick ERG 20 PPI foam.

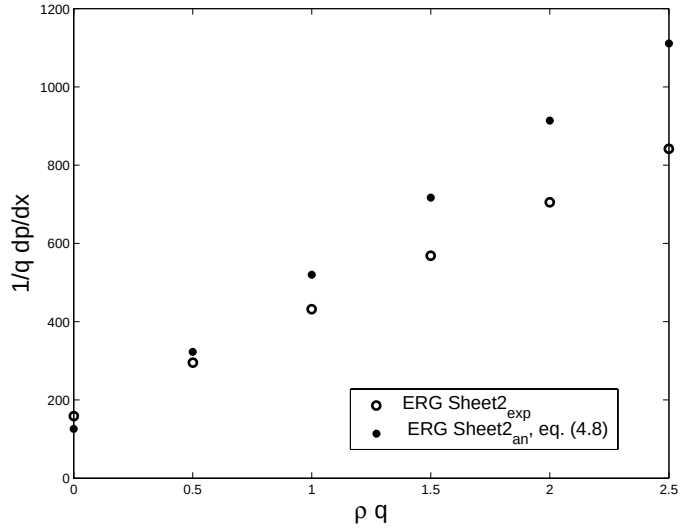

Figure C.2: Comparison between experimental data (Table 4.1) and Crosnier et al. (2006) model with the inertial term given by eq. (4.8) for sheet 2 of a 20mm thick ERG 20 PPI foam.

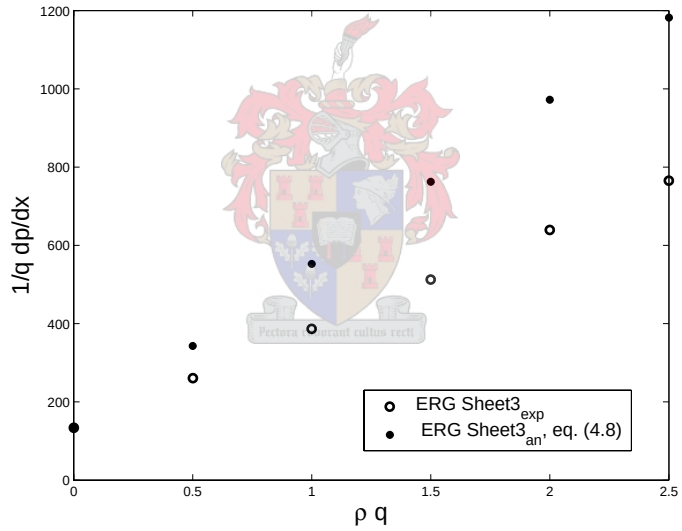

Figure C.3: Comparison between experimental data (Table 4.1) and Crosnier et al. (2006) model with the inertial term given by eq. (4.8) for sheet 3 of a 20mm thick ERG 20 PPI foam.

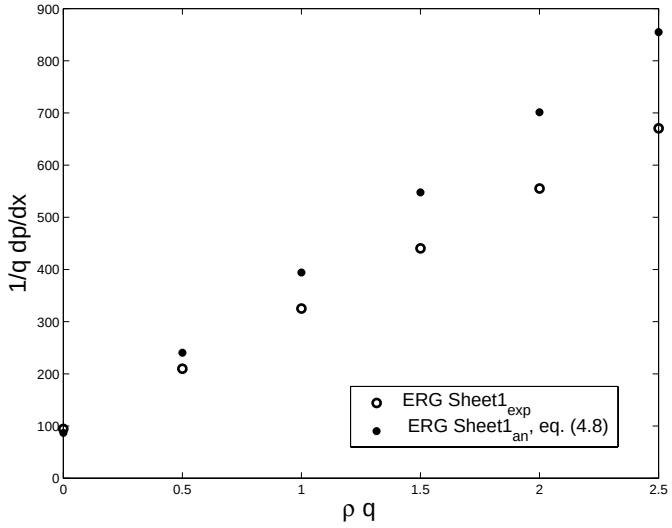

Figure C.4: Comparison between experimental data (Table 4.1) and Crosnier et al. (2006) model with the inertial term given by eq. (4.8) for sheet 1 of a 20mm thick ERG 10 PPI foam.

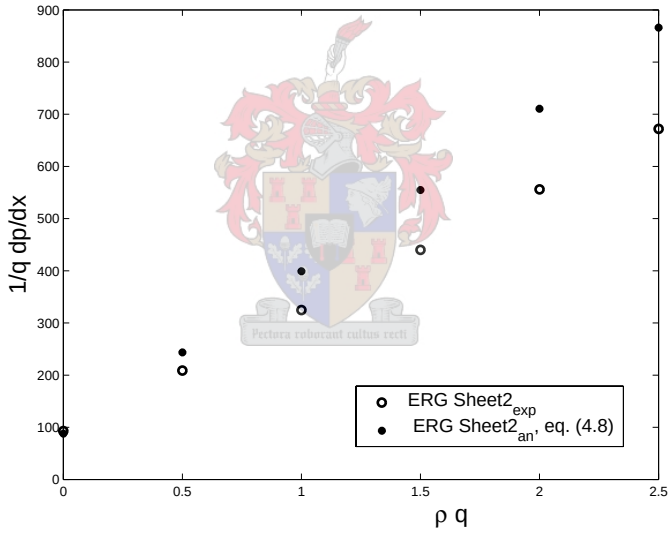

Figure C.5: Comparison between experimental data (Table 4.1) and Crosnier et al. (2006) model with the inertial term given by eq. (4.8) for sheet 2 of a 20mm thick ERG 10 PPI foam.

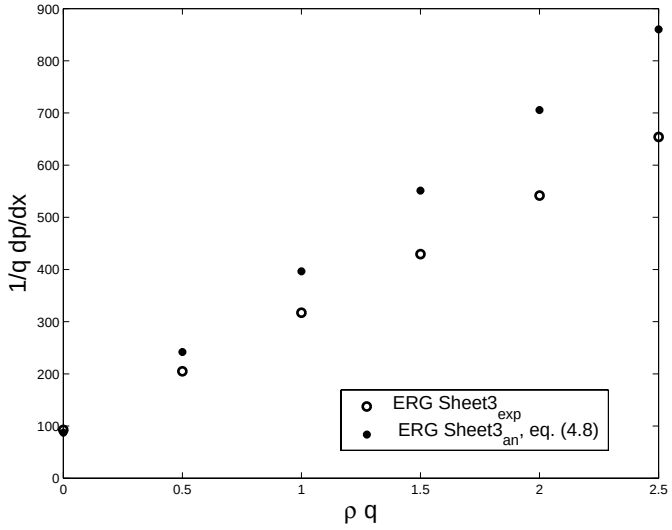

Figure C.6: Comparison between experimental data (Table 4.1) and Crosnier et al. (2006) model with the inertial term given by eq. (4.8) for sheet 3 of a 20mm thick ERG 10 PPI foam.

The correlation between experimental data and the Crosnier et al. (2006) model for a drag coefficient value, $c_d = 1.4$, is depicted in Figures C.7, C.8, C.9, C.10 and C.11.

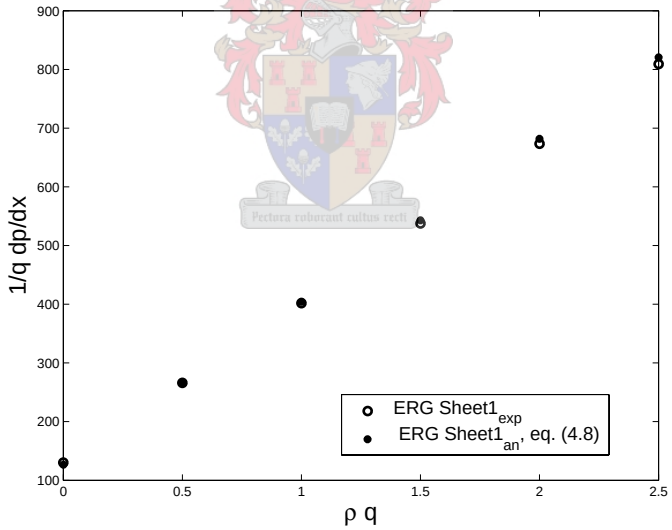

Figure C.7: Comparison between experimental data (Table 4.1) and Crosnier et al. (2006) model with the inertial term given by eq. (4.8) for sheet 1 of a 20mm thick ERG 20 PPI foam.

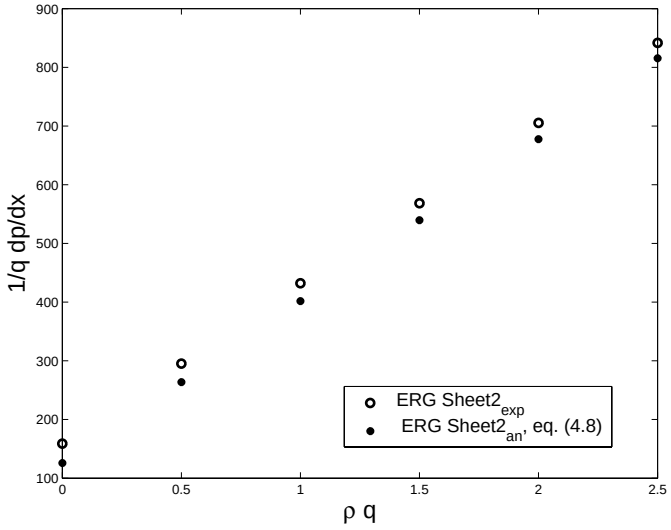

Figure C.8: Comparison between experimental data (Table 4.1) and Crosnier et al. (2006) with the inertial term given by eq. (4.8) for sheet 2 of a 20mm thick ERG 20 PPI foam.

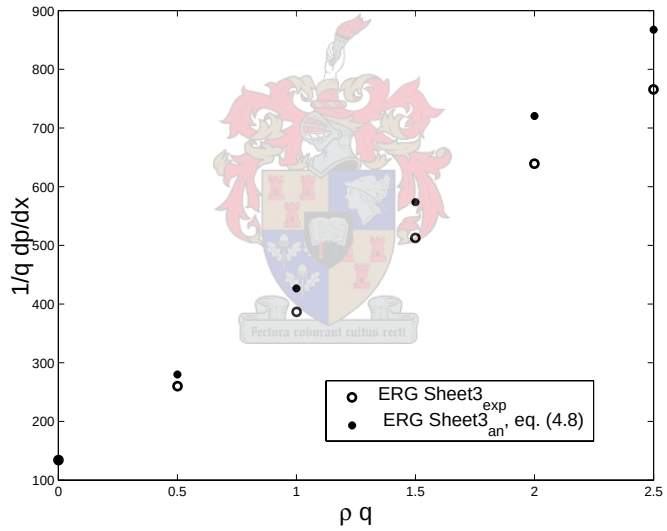

Figure C.9: Comparison between experimental data (Table 4.1) and Crosnier et al. (2006) with the inertial term given by eq. (4.8) for sheet 3 of a 20mm thick ERG 20 PPI foam.

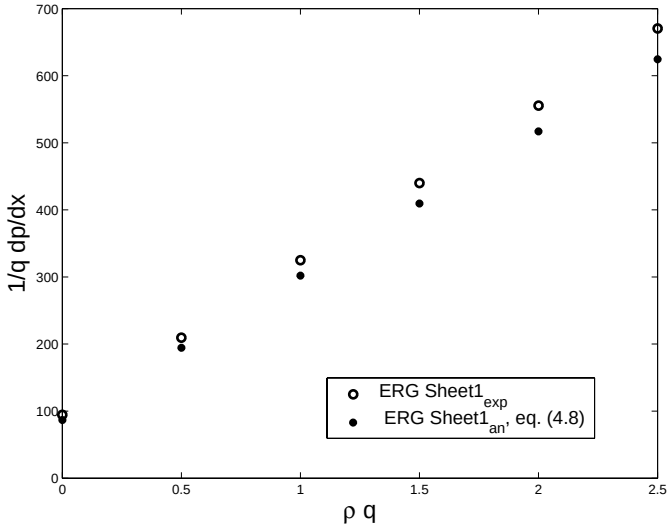

Figure C.10: Comparison between experimental data (Table 4.1) and Crosnier et al. (2006) model with the inertial term given by eq. (4.8) for sheet 1 of a 20mm thick ERG 10 PPI foam.

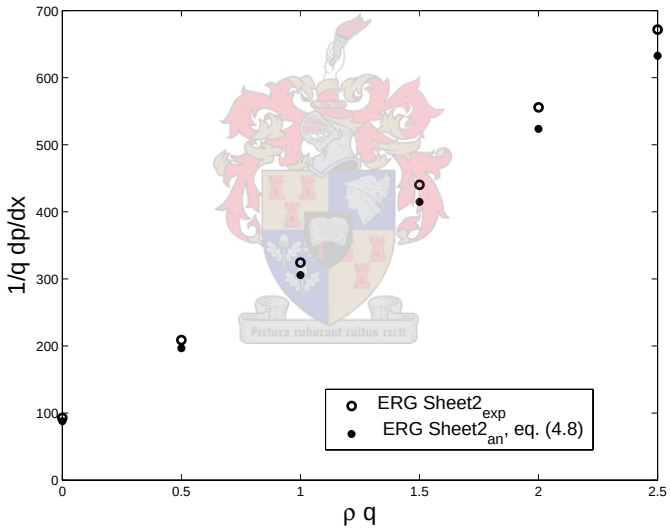

Figure C.11: Comparison between experimental data (Table 4.1) and Crosnier et al. (2006) model with the inertial term given by eq. (4.8) for sheet 2 of a 20mm thick ERG 10 PPI foam.

Appendix D
On the modelling of non-Newtonian purely viscous flow through high porosity synthetic foams

Smit, G.J.F., Du Plessis, J.P. & Wilms, J.M. (2005). On the modelling of non-Newtonian purely viscous flow through high porosity synthetic foams. *Chemical Engineering Science*, 60, 2815-2819.

Appendix E
Modelling of flow in foamlike porous media

Wilms, J.M., Du Plessis, J.P. & Smit, G.J.F. (2005). Modelling of flow in foamlike porous media. *Proceedings of the international conference on environmental fluid mechanics*, 270-276.